学位論文

Thermodynamics and electric field response of water confined in a nanospace
（ナノ空間に拘束された水の熱力学と電場応答）

2024 年 3 月

Yusei Kioka
(木岡 夕星)

Contents

List of Figures

1 Introduction

Water is one of the most familiar materials to us earth dwellers. In fact, water covers makes up about 70% of the earth's surface, and humans themselves are 60% water. The physical properties of water are very unique compared to other materials. For example, the density of water as a solid is lower than that of a liquid, and water usually becomes a liquid when a solid is pressurized. In addition, the boiling point and melting point of water are much higher than those of other hydrogen compounds due to intramolecular hydrogen bonding.

Even though water is so familiar to us, it is not clear whether mankind has clarified all the physical properties of water. It is known that the density of water reaches a maximum of 4°C, but the cause of this is still being investigated through nanoscale analysis [1, 2]. It has also been reported that water near the interface of materials has different physical properties and structures compared to normal water. Derlaguin *et al.* reported that when two glass plates are held together in pure water and water is trapped between them, a large force is required to pull them apart perpendicular to the interface [3]. This repulsive force between the two interfaces is called the disjoining pressure. It is known that water at this interface is less likely to evaporate, has a higher viscosity, and is also less likely to freeze than ordinary bulk water. Peschel and Adlfinger have studied the temperature dependence of this disjoining pressure and found that it has maxima around at $T = 15°\mathrm{C},\ 30°\mathrm{C},\ 45°\mathrm{C},\ 60°\mathrm{C}$ [4]. The structure of the water between the glass plates is thought to change somehow with temperature, causing the change in disjoining pressure, but the specific structure of the water in such a narrow space has not yet been clarified. Recent development of nanotechnology provides new type of nanoscale space confining water, such as the inside of a carbon nanotube (CNT) and the two-dimensional space between the graphene and a substrate. The thermodynamics and dynamical properties

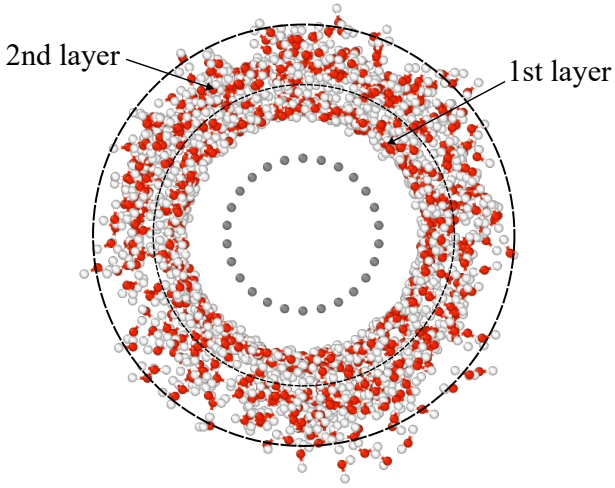

Fig 1. Water around (13,0) SWCNT when the number of water molecules is 1,000 (see Appendix A for definition of (13,0)). The gray spheres represent carbon atoms, the white spheres represent hydrogen atoms, and the red spheres represent oxygen atoms. When there are 1,000 H_2O, the water around the (13,0) SWCNT has the 2-layer structure.

of water in such nanospaces remain to be elucidated. Thus, in this study, we focused on water confined in nanospaces around the surface of carbon materials such as graphene and CNTs [5, 6].

1.1 Water on the carbon materials

Because of its hydrophobicity, water has long been believed not to be adsorbed onto the surface of carbon materials [7]. However, recent experimental and theoretical studies have clarified that water molecular layers are formed on the surfaces of graphene and CNTs even at atmospheric pressure and are thermally stable [8–15]. Homma *et al.* demonstrated the adsorption of water around CNT using two techniques: experiments and the molecular dynamics (MD) simulations [13]. In the experiment, single-walled CNTs (SWCNTs) suspended between silica pillars were prepared and the ambient water vapor pressure and

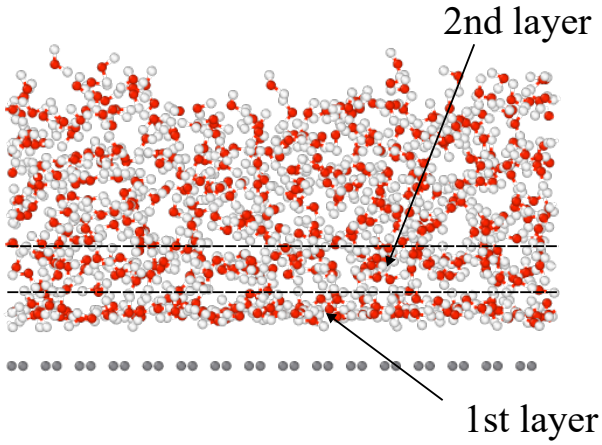

Fig 2. Water on the graphene surface. It has a layered structure, with water from the third layer from the surface onward behaving like bulk water.

temperature were varied. Photoluminescence (PL) spectroscopy emission wavelengths of the SWCNTs showed a sharp redshift of the peak with increasing water vapor pressure. The Raman frequency of the radial breathing mode peak of these SWCNTs was upshifted compared to the vacuum. These results can be attributed to the aggregation of water around the SWCNT. They also used MD simulations to calculate a system with water molecules around a SWCNT at room temperature and found that the water molecules are agglomerated around the SWCNT. The water around the SWCNT has a 2- or 3-layer structure (Fig. 1), which is denser than our well-known bulk water.

Various reports on water on graphite and graphene surfaces have also been made using experiments and simulations. Suzuki *et al.* observed water on graphite surfaces using atomic force microscopy (AFM) [16]. They observed a layer of water in the region of about 1 nm from the graphite interface. Akashi *et al.* used MD calculations to study the structural changes of water on the graphene surface concerning the number of water molecules [14]. The structure of water on the graphene surface is similar to that of water around CNT (Fig. 2), and it changes from a monolayer structure to a bilayer structure as the number of water molecules increases. Maekawa *et al.* also used MD

simulations to simulate water on graphene surfaces and found that the structure of the two-dimensional hydrogen bonding network parallel to the interface has two structures: the ordered polygonal structures and the disordered non-polygonal structures [15]. In the vertical direction, the first layer of interfacial water near the graphene surface and the second layer of interfacial water form a vertical hydrogen bond, and the structure is closed. Therefore, the water on the second layer behaves like bulk water. Kato *et al.* analyzed the data based on the persistent homology method and investigated which structure of the interfacial water on graphene is responsible for the two sub-peaks of the density distribution seen at low temperatures [17]. It was found that their peaks correspond to water clusters with tetrahedral structures existing between the layers of interfacial water. It was also suggested that the rotational motion of these clusters may appear as the peaks due to freezing.

As described above, interfacial water on the carbon materials has different structures and physical properties from bulk water. Among the properties of interfacial water, recent studies have reported interesting thermodynamics and electric field response. First, we will introduce the previous studies on thermodynamics.

1.2 Disappearance of solid–liquid phase transition point of interfacial water around a carbon nanotube (CNT)

The interfacial water around a CNT exhibits peculiar thermodynamic properties that differ from those of bulk water. Saito *et al.* used PL spectroscopy to measure the dielectric constant of the interfacial water around various semiconductor CNTs in the temperature range from -130°C to 20°C [18]. If the interfacial water around CNT exhibits a solid–liquid phase transition at 0°C like bulk water, its dielectric constant should change discontinuously at 0°C. However, the dielectric constant of the interfacial water changed continuously

even when the temperature was lowered to −130°C. Therefore, they concluded that the interfacial water around CNT does not show solid–liquid phase transition even at −130°C. However, the structure of water in this temperature range of −130°C to 20°C (hereafter referred to as the *solid–liquid crossover region*) has not yet been clarified.

1.3 The extremely small dielectric constant of confined water between graphene and hexagonal boron nitride (h-BN) substrates

Next, we introduce the previous study on the electric field response of interfacial water. According to the experiment of the previous study, the dielectric constant of water with a thickness of about 1 nm confined in the nanospace between the hexagonal boron nitride (h-BN) substrate and graphene, measured by scanning dielectric microscopy based on electrostatic force detection with an AFM [19], was $\varepsilon \sim 2.1$ [20]. This is an extremely small value compared to that of bulk water at room temperature ($\varepsilon_{\mathrm{r}}^{\mathrm{bulk}} \sim 80$) [21, 22]. As the thickness of the confined water is increased, the dielectric constant of the confined water gradually increases and approaches that of bulk water at about 200 nm. In the previous study, it was hypothesized that this is due to the existence of a structure with restricted rotational degrees of freedom in the water near the surfaces, but this remains to be elucidated.

The dielectric properties of the water confined between the substrate and the graphene are important properties for the realization of graphene field-effect transistors (FETs). Graphene is attracting attention as a substitute for silicon as the channel material in FETs because it exhibits high mobility [23–25]. Nagashio *et al.* have reported that, when water exists in the nanospace between the graphene layer and substrate of a graphene FET, it strongly influences the FET's characteristics [26]. That is, the characteristics of the graphene FET are affected by the dielectric properties of the confined water.

1.4 Purpose of this study

As described above, there are unresolved issues in the thermodynamics and electric field response of water at surfaces. In this study, we use simulations to clarify the thermodynamics, which is a static property of interfacial water, and the electric field response, which is related to the dynamics of interfacial water. Therefore, we have the following two objectives.

1. To clarify the structure and dynamics of interfacial water around CNT in the solid–liquid crossover region.

2. To elucidate the physical origin of the dielectric properties of confined water between graphene and h-BN.

This thesis is organized in the following sections. Section 2 introduces the MD method, the simulation technique used in this study. Section 3 describes our work on the thermodynamics of interfacial water around CNT in the solid–liquid crossover region. Section 4 describes the dielectric properties of water confined in the nanospace between graphene and h-BN substrate. Section 5 provides a summary of the overall study.

2 Molecular dynamics (MD) simulation method

MD simulation method is a method for determining the motion of atoms and molecules by numerically solving Newton's equations of motion using forces acting between them. Compared to quantum mechanical, such as first-principles calculations based on density functional theory, classical MD simulations require less computation time and can handle larger systems. There are also methods such as the finite element method, which divides a continuum into meshes and solves partial differential equations, that can be used for very large systems of 100 nm or more. However, this method cannot simulate structural data such as the polarization and hydrogen bonding of water molecules, nor can it simulate the dynamics of water molecules. Therefore, in this study, we used classical MD simulations, which are not too computationally demanding and can observe the structure and dynamics of water. In this chapter, we explain the MD method used in this study.

2.1 Velocity-Verlet algorithm

In MD simulations, the Newton's equation of motion for a particle with mass m is given by

$$m\frac{d^2\boldsymbol{r}_i(t)}{dt^2} = \boldsymbol{F}_i(t). \tag{1}$$

Here $\boldsymbol{F}_i(t)$ is the force applied to particle i at time t, which is the combined force of the interaction between the particles and external forces such as the electric field. Since the positional relationship between particles changes with time t, the interaction between particles is time-dependent. In general, it is necessary to solve a complex set of differential equation for a many-body system. Therefore, it can be simplified by replacing the left-hand side with a Taylor series expansion of the difference equation. The Taylor expansion of the coordinates $\boldsymbol{r}_i(t + \Delta t)$ and the velocity $\boldsymbol{v}_i(t + \Delta t)$ from time t to Δt after Δt is performed around $\Delta t = 0$, and the approximation up to the second order term gives the following

expression

$$\boldsymbol{r}_i(t+\Delta t) = \boldsymbol{r}_i(t) + \frac{d\boldsymbol{r}_i(t)}{dt}\Delta t + \frac{1}{2!}\frac{d^2\boldsymbol{r}_i(t)}{dt^2}\Delta t^2 + O(\Delta t^3), \tag{2}$$

$$\boldsymbol{v}_i(t+\Delta t) = \boldsymbol{v}_i(t) + \frac{d\boldsymbol{v}_i(t)}{dt}\Delta t + \frac{1}{2!}\frac{d^2\boldsymbol{v}_i(t)}{dt^2}\Delta t^2 + O(\Delta t^3). \tag{3}$$

From $d\boldsymbol{r}_i(t)/dt = \boldsymbol{v}_i(t)$ and Eq. (1), Eq. (2) and Eq. (3) can be transformed as follows

$$\boldsymbol{r}_i(t+\Delta t) = \boldsymbol{r}_i(t) + \boldsymbol{v}_i(t)\Delta t + \frac{\boldsymbol{F}_i(t)}{2m}\Delta t^2 + O(\Delta t^3), \tag{4}$$

$$\boldsymbol{v}_i(t+\Delta t) = \boldsymbol{v}_i(t) + \frac{\boldsymbol{F}_i(t)}{m}\Delta t + \frac{1}{2m}\frac{d\boldsymbol{F}_i(t)}{dt}\Delta t^2 + O(\Delta t^3). \tag{5}$$

We perform a Taylor expansion around $\Delta t = 0$ concerning $\boldsymbol{F}_i(t+\Delta t)$ and make an approximation up to the first-order term, we obtain

$$\boldsymbol{F}_i(t+\Delta t) = \boldsymbol{F}_i(t) + \frac{d\boldsymbol{F}_i(t)}{dt}\Delta t + O(\Delta t^2), \tag{6}$$

$$\frac{d\boldsymbol{F}_i(t)}{dt} = \frac{\boldsymbol{F}_i(t+\Delta t) - \boldsymbol{F}_i(t)}{\Delta t} + O(\Delta t^2). \tag{7}$$

Thus, Eq. (5) can be transformed as follows

$$\boldsymbol{v}_i(t+\Delta t) = \boldsymbol{v}_i(t) + \frac{1}{2m}\left(\boldsymbol{F}_i(t+\Delta t) + \boldsymbol{F}_i(t)\right)\Delta t + O(\Delta t^3). \tag{8}$$

The Velocity-Verlet algorithm provides initial coordinates $\boldsymbol{r}_i(0)$ and initial velocity $\boldsymbol{v}_i(0)$ and solves Eq. (4) and Eq. (8) to obtain coordinate and velocity data for Δt intervals [27]. First, substitute $\boldsymbol{r}_i(0)$ and $\boldsymbol{v}_i(0)$ into Eq. (4) to obtain $\boldsymbol{r}_i(0+\Delta t)$. Substitute this coordinate into the potential function and calculate $\boldsymbol{F}_i(0+\Delta t)$, which is then substituted into Eq. (8) to obtain $\boldsymbol{v}_i(0+\Delta t)$. By repeating the above method, the coordinates and velocity data for each time step Δt are calculated by the MD calculation.

2.2 Lennard–Jones potential

Since MD method involves solving the equations of motion for each atom, the force exerted on each atom must be described. This interaction between atoms is given by a potential function$\phi(\boldsymbol{r})$, which is expressed as follows

$$\boldsymbol{F}_i = -\frac{\partial \phi(\boldsymbol{r}_i)}{\partial \boldsymbol{r}_i}. \tag{9}$$

The Lennard–Jones (LJ) potential $\phi_{\mathrm{LJ}}(r)$ is a widely used potential function that describes the interaction between two atoms. This potential is written as

$$\phi_{\mathrm{LJ}}(r) = 4\varepsilon \left[\left(\frac{\sigma}{r}\right)^p - \left(\frac{\sigma}{r}\right)^q \right], \tag{10}$$

where r is the distance between the two atoms, σ has the dimension of length, and ε has the dimension of energy. σ is the value that defines the distance between the atoms, which is the minimum of the potential function, with a minimum at $2^{\frac{1}{6}}\sigma$, and $-\varepsilon$ is its minimum value. The first term indicates repulsion due to overlapping electron clouds, and the second term indicates attraction due to permanent dipoles and London dispersion forces. The exponential part of each term is called the (q, p) potential. In this study, the representative (6,12) potential is used. In the following, we will discuss the Universal Force Field (UFF) [28] and SPC/E potentials [29], which are used as LJ potentials in this study.

2.2.1 Universal Force Field (UFF) potential

Rappe *et al.* created the UFF potential, a generic force field of the LJ potential type covering almost all elements in the periodic table [28]. The original work describes σ and ε between homogeneous elements. The parameters of the UFF potential between dissimilar elements A and B are calculated using the Lorentz-Berthelot combining role

below,

$$\varepsilon_{\mathrm{AB}} = \sqrt{\varepsilon_{\mathrm{A}}\varepsilon_{\mathrm{B}}}, \tag{11}$$

$$\sigma_{\mathrm{AB}} = \frac{\sigma_{\mathrm{A}} + \sigma_{\mathrm{B}}}{2}, \tag{12}$$

where $\varepsilon_{\mathrm{A}}, \sigma_{\mathrm{A}}, \varepsilon_{\mathrm{B}}$ and σ_{B} are parameters of the LJ potentials of elements A and B, respectively.

2.2.2 SPC/E potential

In this study, we used the SPC/E (extended single point charge) model, which is a rigid body model as water molecules, for our simulations [29]. The SPC/E potential $\phi(r)$, which describes the interaction between water molecules, is divided into intermolecular force $\phi_{\mathrm{LJ}}(r)$ and electrostatic interaction terms $\phi_{\mathrm{q}}(r)$ and is expressed as follows

$$\phi(r) = \phi_{\mathrm{LJ}}(r) + \phi_{\mathrm{q}}(r). \tag{13}$$

The intermolecular forces $\phi_{\mathrm{LJ}}(r)$ are indicated by the following LJ potentials

$$\phi_{\mathrm{LJ}}(r) = \frac{A}{r^{12}} - \frac{B}{r^{6}}, \tag{14}$$

where $A = 0.37122\ (\mathrm{kJ/mol})^{1/6} \cdot \mathrm{nm}$ and $B = 0.3428\ (\mathrm{kJ/mol})^{1/12} \cdot \mathrm{nm}$. The electrostatic potential is defined as

$$\phi_{\mathrm{q}}(r) = \sum_{j} \frac{1}{4\pi\varepsilon_0} \cdot \frac{q_i q_j}{r_{ij}}. \tag{15}$$

The model gives charges on oxygen and hydrogen of -0.8476 eC and 0.4238 eC, respectively. The hydrogen-oxygen spacing is 0.1 nm and the angle HOH is 109.47°.

The SPC/E model has density (Exp : $0.9970\ \mathrm{g/cm^3}$ [30], SPC/E : $0.9984\ \mathrm{g/cm^3}$ [30]) and self-diffusion coefficients (Exp : $2.2990\ \mathrm{m^2/s}$ [31], SPC/E : $2.7849\ \mathrm{m^2/s}$ [32]) that are closer to experimental values than the TIP3P model, which is also a three-site model.

The melting point of ice Ih (hexagonal ice crystal) in the SPC/E model is 279 K $\pm$ 5K in the MD calculation with the Ewald sum, which is close to the melting point of real ice [33]. Four-site models such as TIP4P with one negatively charged dummy atom added [34] and five-site models such as TIP5P with two added [35] can give more accurate melting points and dielectric properties, but the SPC/E model is superior in computational efficiency. In this study, we used the SPC/E model because the motion of many water molecules is calculated for a long time.

2.3 Nosé–Hoover thermostat

In order to perform MD in the canonical ensemble (NVT ensemble), a thermostat is introduced to control the temperature of a system. There are several thermostat methods that can add and remove energy from an MD system. In this work, we adopted the Nosé–Hoover thermostat. The Nosé-Hoover thermostat represents the energy exchange with a virtual heat bath by introducing a new dynamical variable, s [36, 37]. The velocity vector and time variables are as follows

$$t' = \frac{t}{s}, \tag{16}$$

$$\boldsymbol{v}_i' = s\dot{\boldsymbol{r}}_i, \tag{17}$$

where t' and v' are the time and velocity in the real system, and t is the time in the extended-system, which includes both the real system and the heat bath. In the following explanations in this chapter, primed variables refer to variables in the real system. As the value of s changes, the velocity of the real system changes, and the temperature also changes, representing the exchange of thermal energy between the real system and the heat bath. As the value of s changes, the velocity of the real system changes, and the temperature also changes, representing the exchange of thermal energy between the real system and the heat bath. Since a change in the value of s results in a change in the velocity of the real system and a temperature change, it can be used to describe the exchange of thermal energy between the system and the heat bath. The Lagrangian $\mathcal{L}$ of N atoms in this extended system is defined as

$$\mathcal{L} = \sum_{i=1}^{N} \frac{1}{2} m_i s^2 \dot{\boldsymbol{r}}_i^2 - E + \frac{Q}{2}\dot{s}^2 - g k_{\mathrm{B}} T \ln s, \tag{18}$$

where Q is the mass of the heat bath and g is the degree of freedom of the system, $g = 3N + 1$. The third term represents the kinetic energy of s and the fourth term

represents the potential energy of s. The Euler–Lagrange equation is used to derive the following equations of motion, which are solved by MD calculations

$$m_i \ddot{\boldsymbol{r}}_i = -\frac{1}{s^2}\frac{\partial E}{\partial \boldsymbol{r}_i} - m_i \frac{2\dot{s}}{s}\dot{\boldsymbol{r}}_i, \tag{19}$$

$$Q\ddot{s} = \sum_{i=1}^{N} m_i s \dot{\boldsymbol{r}}_i^2 - \frac{g k_B T}{s}. \tag{20}$$

The distribution function of this extended-system is known to be consistent with the canonical ensemble [36, 37].

2.4 Long range coulomb interaction

The interaction between two charged particles separated by a distance r in the MD calculation is as follows

$$E = \phi(r) + \sum_j \frac{1}{4\pi\varepsilon_0} \cdot \frac{q_i q_j}{r_{ij}}, \tag{21}$$

where the first term is the potential function and the second term is the Coulomb interaction. Since both the potential function and the Coulomb interaction will have values no matter how large r is, the cutoff distance r_c is determined and the interaction is calculated only in the range $r < r_c$. However, considering that the Coulomb interaction is inversely proportional to r and thus decays slowly, while the radial distribution of the number of particles increases by $4\pi r^2 \Delta r$, we cannot ignore the Coulomb interaction at a distance. Therefore, the Ewald method [38] and the particle-particle-particle-mesh (PPPM) method [39] are two methods to calculate the long-range Coulomb interaction.

The Ewald method can handle interactions at long distances by splitting the Coulomb interaction into two components that converge quickly in reciprocal space and real space. Specifically, the former replaces the actual charge distribution with a spatially extended one, such as a Gaussian distribution, and the latter is the difference between the actual charge distribution and its spatially extended distribution. The Coulomb interaction ϕ_q in the Ewald method is

$$\phi_q = E_r + E_k + E_s + E_d, \tag{22}$$

where E_r represents the difference between the actual charge distribution and the spread distribution that converges quickly in real space, and E_k corresponds to the spread charge distribution with Gaussian distribution that converges quickly in reciprocal space The E_s is the term that subtracts the Gaussian distribution of its charge and E_d is the correction

term. If there are N charges in a cell of volume $V = L^3$, they are each described as follows

$$E_r = \frac{1}{2} \sum_{\boldsymbol{n} \in \mathbb{Z}^3} \sum_{i=1}^{N} \sum_{j=1}^{N} q_i q_j \frac{\mathrm{erfc}(\alpha |\boldsymbol{r}_{ij} + L\boldsymbol{n}|)}{|\boldsymbol{r}_{ij} + L\boldsymbol{n}|}, \tag{23}$$

$$E_k = \frac{1}{2L^3} \sum_{\boldsymbol{k} \neq 0} \frac{4\pi}{k^2} e^{-k^2/4\alpha} |\tilde{\rho}(\boldsymbol{k})|^2, \tag{24}$$

$$E_s = -\frac{\alpha}{\sqrt{\pi}} \sum_{i=1}^{N} q_i^2, \tag{25}$$

$$E_d = \frac{2\pi}{(1 + 2\varepsilon')L^3} \left(\sum_{i=1}^{N} q_i \boldsymbol{r}_i \right)^2. \tag{26}$$

where $\boldsymbol{n}$ is a 3-dimensional vector indicating the number of image cells due to periodic boundary conditions, $\boldsymbol{k}$ is the wave number, and $\tilde{\rho}$ is the Fourier transform of the charge density. The $1/4\pi\varepsilon_0$ is omitted. The α is a parameter with the inverse dimension of the length and is called the Ewald parameter. The complementary error function $\mathrm{erfc}(x)$ is defined by

$$\mathrm{erfc}(x) = \frac{2}{\sqrt{\pi}} \int_x^{\infty} \exp(-t^2) dt. \tag{27}$$

Because the convergence of the complementary error function is fast, E_r converges quickly in real space.

The Ewald method, which converges quickly even over long distances, can be used to calculate long-range Coulomb interactions, but it is computationally expensive. In the PPPM method, E_k is calculated by mesh chopping the space and using the Fast Fourier Transform to speed up the calculation. Each point charge is assigned to a mesh point specified by the charge assignment function W. In LAMMPS [40], the MD package used in this study, the kspace_style command can be used to specify the calculation method for the long-range Coulomb interaction. The time complexity of the Ewald method requires $O(N^{3/2})$, where N is the number of particles, while the PPPM method requires $O(N \log N)$, which is shorter than the Ewald method.

3 Thermodynamics of interfacial water around CNT, a static property of water

3.1 Introduction

Recently, Saito *et al.* confirmed experimentally using a PL spectroscopy experiment that the dielectric constant of the interfacial water around a CNT varies linearly in a wide temperature range from $-130°C$ to $20°C$ [18]. This indicates that the interfacial water around a CNT does not undergo a clear solid–liquid phase transition, in contrast to bulk water, which exhibits a transition at $0°C$. However, the microscopic structure of interfacial water in the solid–liquid crossover region remains to be elucidated.

In order to clarify this issue, we focused attention on the dynamics of the interfacial water in the solid–liquid crossover region, because the crossover can be characterized by a change in the degrees of freedom of the molecular motion. Thus, we performed MD simulation for the interfacial water around a CNT and calculated the rotational autocorrelation function (RACF) for the water molecules [41, 42]. In this section, we present a new picture of the interfacial water around a CNT: the coexistence of slow and fast dynamics in the interfacial water. Finally, we conclude that the origin of the slow and fast dynamics is related to the water molecules in domains, consisting of polygonal water clusters, and those in the domain wall areas, respectively.

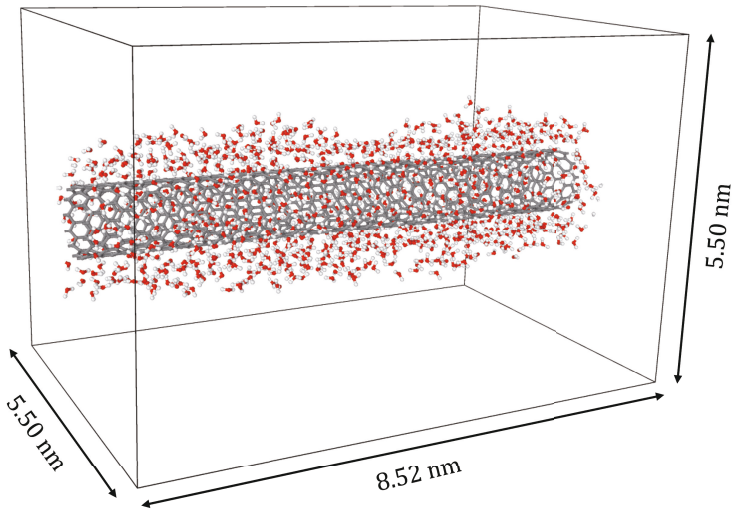

Fig 3. Simulation cell for MD calculations. It contains a (13,0) SWCNT (gray tube) with 1,000 adsorbed H_2O molecules (red spheres are oxygen atoms and white spheres are hydrogen atoms). Copyright 2023 The Japan Society of Applied Physics [43]

3.2 Simulations setting

We used LAMMPS (3 Mar 2020 [40]) to perform MD simulations based on the NVT ensemble to obtain the thermal equilibrium states of water around a CNT. As an initial state, 1,000 H_2O molecules were randomly distributed around a (13,0) SWCNT (see Appendix A for definition of (13,0)) placed in a simulation box with dimensions of $5.50 \times 5.50 \times 8.52$ nm^3 and with periodic boundary conditions imposed in the (x, y, z) directions (Fig. 3). The direction of the SWCNT is parallel to the z axis. The Nosé–Hoover thermostat was used to control the temperature of the system [36, 37]. As force fields, we used SPC/E for the water model [29] and UFF for the interaction between a water molecule and a carbon atom [28]. The equation of motion was numerically solved by the Velocity-Verlet method [27] with a time step $\Delta t = 1.0$ fs. The long-range Coulomb interactions were treated by the PPPM method [39]. The calculations were carried out for up to 570 ns until thermal equilibrium was reached. The RACF is represented by the time correlation

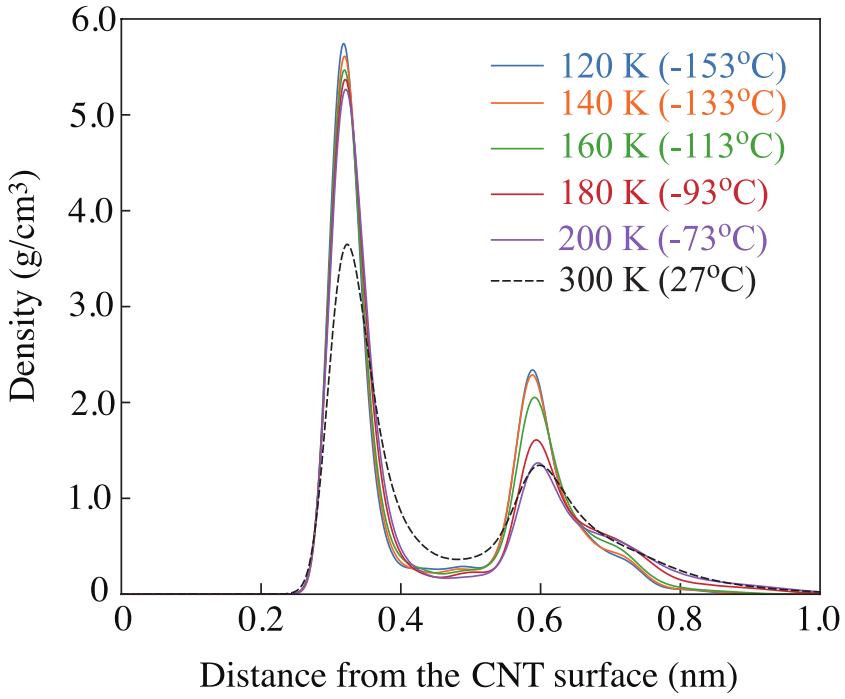

Fig 4. Distributions of oxygen atoms in water molecules along radial direction of the (13,0) SWCNT at T = 120 K (−153°C), 140 K (−133°C), 160 K (−113°C), 180 K (−93°C), 200 K (−73°C), and 300 K (27°C). The origin of the horizontal axis was set as the (13,0) SWCNT surface. Copyright 2023 The Japan Society of Applied Physics [43].

function of the dipole and is defined as

$$\begin{aligned} C_{\mathrm{R}}(t) &= \frac{1}{2}\langle 3\cos^2\theta_i(t) - 1\rangle \\ &= \frac{1}{2}\left\langle 3\left(\frac{\boldsymbol{p}_i(t)\cdot\boldsymbol{p}_i(0)}{|\boldsymbol{p}_i(t)||\boldsymbol{p}_i(0)|}\right)^2 - 1\right\rangle, \end{aligned} \tag{28}$$

where $\boldsymbol{p}_i(t)$ is the electric dipole moment for the i-th water molecule and $\theta_i(t)$ is the angle between $\boldsymbol{p}_i(t)$ and $\boldsymbol{p}_i(0)$. In Eq. (28), the angle bracket represents an ensemble average concerning various initial states. The parameter $\{\boldsymbol{p}_i(t)\}$ can be calculated by MD simulation.

3.3 Results and discussion

3.3.1 Density distribution of interfacial water around CNT

Figure 4 represents the distributions of oxygen atoms in water molecules along the radial direction of the CNT for various temperatures. The origin of the horizontal axis was set as the CNT surface. As can be seen, a double-layer structure is always observed within the 120 K (−153°C)≤ T ≤ 300 K (27°C) range that was simulated. The first and second peaks increase and the linewidth of the second peak decreases with decreasing temperature. This behavior agrees with results obtained in previous studies in which water layers were formed on graphene [15, 17]. Due to the steric hindrance of the CNTs, the OH bonds of the water molecules in the first layer cannot orient toward the surface of the CNT, but instead orient parallel to the surface and form hydrogen bonds with neighboring water molecules. The other OH bond of these water molecules forms a hydrogen bond with another water molecule in the same plane or orients away from the CNT surface. OH bonds oriented away from the CNT surface can form hydrogen bonds with water molecules in the second layer. Thus, the water molecules in the first and second layers are bonded in a complementary fashion, forming a stable structure with hydrogen bonds that is "closed" within the two layers.

3.3.2 RACF for bulk water and interfacial water around CNT

Figure 5(a) shows the RACF for bulk water at T = 120 K (−153°C), 140 K (−133°C), 260 K (−13°C), 280 K (7°C), and 300 K (27°C) as a function of time. The black curve is the result of a least-squares fit of the RACF results to an exponential function with a constant term. Each curve relaxes to a constant value in the limit of long time. From Fig. 5(a), it can be seen that the RACF for bulk water shows a long time correlation at low temperatures, but the correlation is lost in a short time above 0°C. This abrupt change in

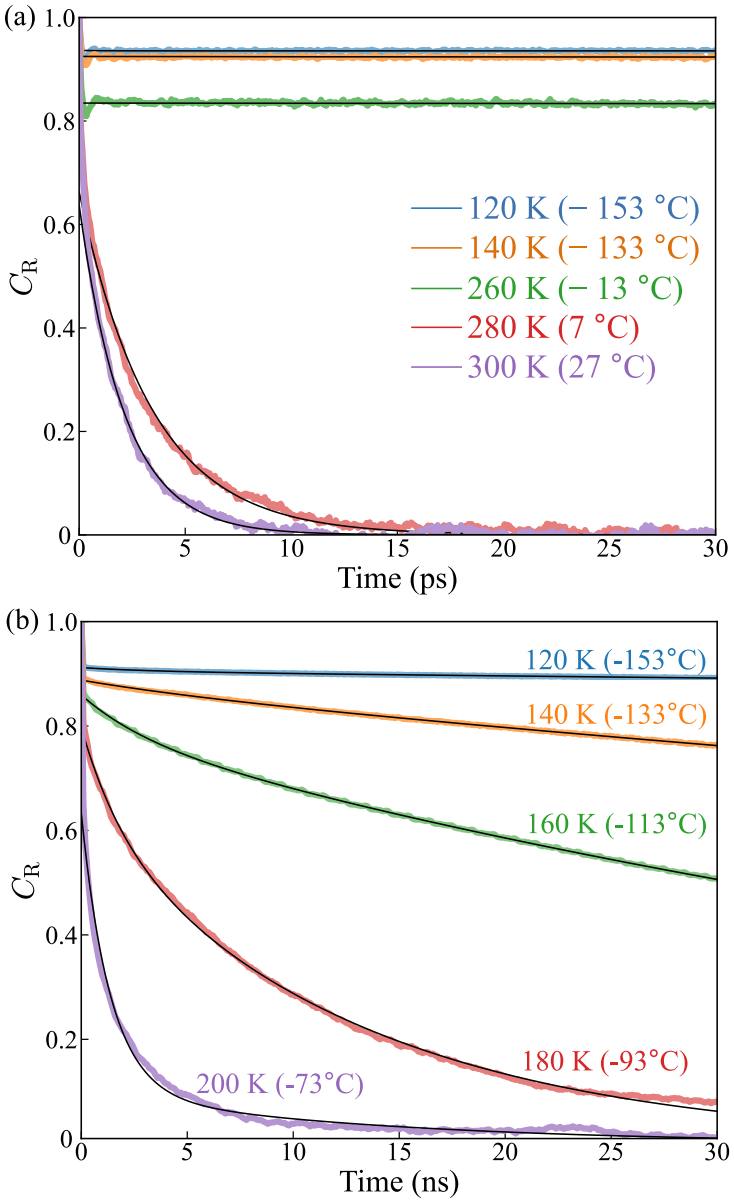

Fig 5. (a) RACF for bulk water at T = 120 K (−153°C), 140 K (−133°C), 260 K (−13°C), 280 K (7°C), and 300 K (27°C) as a function of time. Black lines are fitting curves obtained from a single exponential function with a constant term. (b) RACF for the interfacial water around the (13,0) SWCNT at T = 120 K (−153°C), 140 K (−133°C), 160 K (−113°C), 180 K (−93°C), and 200 K (−73°C) as function of time. Black lines are fitting curves obtained with Eq. (29). [43].

correlation time means that the bulk water shows a solid–liquid phase transition near 0°C in the present MD simulation with the SPC/E force field, which is consistent with previous work [33, 44].

Similarly, Fig. 5(b) shows the RACF for interfacial water around the CNT surface at several temperatures (T = 120 K (−153°C), 140 K (−133°C), 160 K (−113°C), 180 K (−93°C), and 200 K (−73°C)) as a function of time. In contrast to Fig. 5(a), the change in the correlation in Fig. 5(b), shows a continuous decrease with increasing T. The gradual change in the correlation for the interfacial water around the CNT is totally different from that for the bulk water. This suggests that the interfacial water around a CNT does not undergo a clear solid–liquid phase transition but rather exhibits a solid–liquid crossover. The changes in the terminal value of each RACF are also significantly different (Appendix B). These MD results are consistent with the results of recent experiments based on PL spectroscopy [18].

It should be noted that $C_{\mathrm{R}}(t)$ for bulk water relaxes three orders of magnitude faster than that for interfacial water around a CNT. From Figs. 5(a) and 5(b), it can be seen that the relaxation time of water around CNT is much longer than that of bulk water and continues to fall even in the extended time calculation of t = 30 ns. This extremely long relaxation time means that the rotational degrees of freedom of CNT-adsorbed water are more limited than in bulk water, even near room temperature. Conversely, the fact that CNT-adsorbed water has a finite relaxation time even at low temperatures suggests that the water molecules are not completely frozen.

These results are in good agreement with the timescale of the rotational motion of water at the polar interface [45, 46]. Fig. 6 shows a schematic diagram of the water structure at the polar interface and the timescale of rotational relaxation in each region. The water is divided into three regions from the vicinity of the polar interface. There is no uniform way to name the water in each region, and the representative names are listed. The

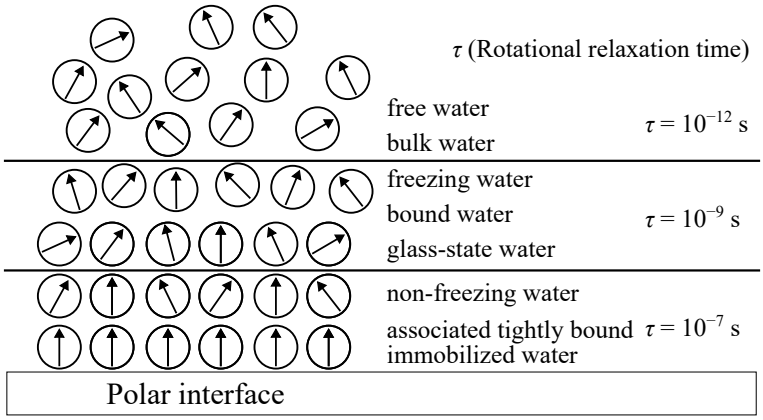

Fig 6. Schematic diagram of the structure of water at the polar interface. Circles indicate water molecules and arrows indicate polarization. The names of each region are not uniform, and representatives are listed. The τ denotes the relaxation time of the rotational motion.

relaxation time of RACF for water around CNT is about a few ns, a timescale close to that of freezing water in Fig. 6. For bulk water, it is about a few ps, which is also the relaxation time of bulk water in Fig. 6. Since the CNT is a non-polar interface, the water at the CNT interface is not as strongly constrained as the water near the polar interface (non-freezing water, which slows down the rotation significantly), but it is somewhat constrained by van der Waals forces, so it is expected to relax similarly to the freezing water in the second layer from the polar interface.

3.3.3 Coexistence of slow and fast dynamics in interfacial water around CNT

To analyze the results of the RACF for the interfacial water around the CNT and bulk water shown in Fig. 5, we performed curve fitting for each results. Assuming that the rotational correlation is a Markov process that depends only on the immediately preceding state, the rotational autocorrelation function is represented by an exponential function. In addition, it is known that in ordinary non-glassy liquids, the typical time-dependent correlation function exhibits an exponential relaxation with a single time constant, the

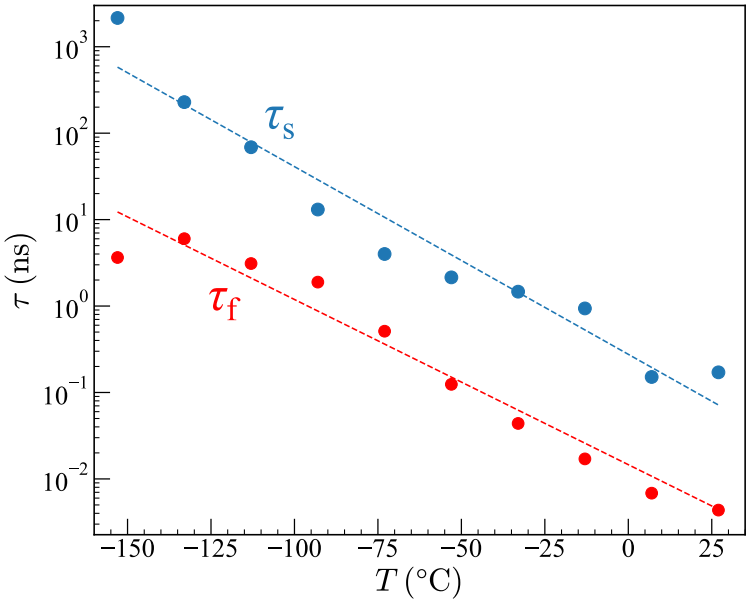

Fig 7. Temperature dependence of time constants τ_s (blue marks) and τ_f (red marks). The blue and red dashed lines are the fitting curves obtained by exponential fitting of the τ_s and τ_f results, respectively. Copyright 2023 The Japan Society of Applied Physics [43].

so-called Debye-relaxation [47,48]. We fitted the RACF results with a single exponential function; the RACF for bulk water could be fitted, but not that for interfacial water. Therefore, we assumed that a double exponential (double exp) function with two different time constants could be used for fitting, and we used the least-squares method to fit the RACF results with double exp functions. The double exp functions can be expressed by

$$C_R(t) = A_s \exp\left(-\frac{t}{\tau_s}\right) + A_f \exp\left(-\frac{t}{\tau_f}\right), \tag{29}$$

where A_s, A_f, τ_s, and τ_f are the fitting parameters. The subscripts represent slow and fast. A_s and A_f correspond to the amount of water molecules with fast and slow relaxation of rotational correlations. τ_s and τ_f are the time constants.

The black lines of Fig. 5(b) are the results of fitting the RACF for the interfacial water by the double exp function (Eq. (29)), and the fit is good at all temperatures, with R^2 values in the range of about 0.90 to 0.99.

Figure 7 shows the temperature dependence of the time constants τ_s (blue marks) and

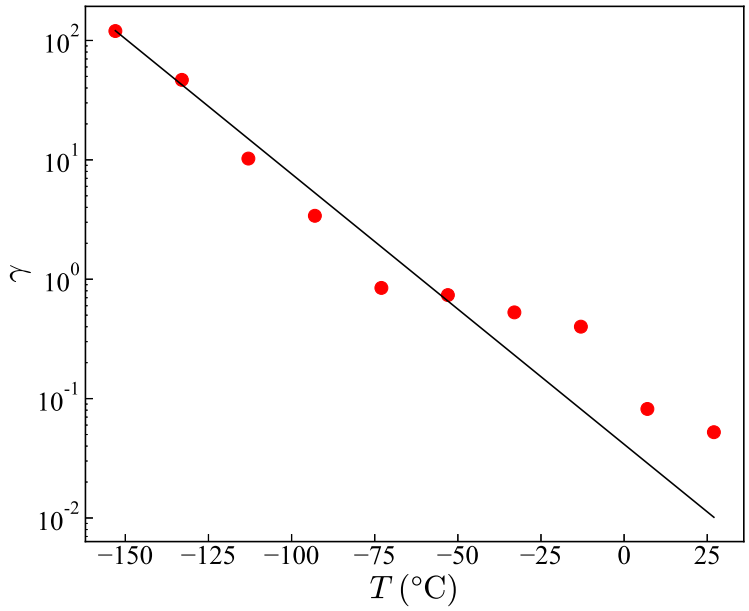

Fig 8. Variation of γ (the ratio of A_f to A_s) with temperature. A larger γ indicates a larger proportion of water molecules with slow relaxation. The black line is the fitting curve obtained with an exponential function. Copyright 2023 The Japan Society of Applied Physics [43].

τ_f (red marks) of the double exp function (Eq.(29)). Both the dashed lines are the result of exponential fitting of the τ_s and τ_f results, with the blue dashed line corresponding to τ_s and the red dashed line to τ_f. It can be seen that the values of both τ_s and τ_f tend to decrease exponentially with increasing temperature, and in particular that τ_s is two orders of magnitude higher than τ_f. This suggests that it is reasonable to separate the two exponential functions of the double exp function into slow and fast relaxation terms.

The fact that the interfacial water around a CNT can be fitted with a double exp function is due to the structure of hydrogen bonds in the interfacial water. We now recognize that the double-layer structure of interfacial water around a CNT in Fig. 4 is similar to that of on graphene obtained in our previous works [15, 17]. In the previous work based on MD simulation, we have reported that such water layers form hydrogen bonds in a plane parallel to the graphitic surfaces, and that the bond structure consists of two types: ordered

structures (polygons) and disordered structures (non-polygons) [15,17]. Other groups also showed that stable polygonal water clusters appear on the graphitic surface [49–52], using ab initio simulations based on density functional theory.

It is speculated that the first term in Eq. (29) corresponds to the ordered structures and the fast relaxation term corresponds to the disordered structures, but it is not clear whether the dynamics and the interfacial water binding structures really correspond. Therefore, since the size of the ordered structure is expected to decrease with increasing temperature, we investigated the temperature dependence of $\gamma = A_s/A_f$, which is the ratio of the amount of slow-converging water molecules to the amount of fast-converging water molecules. Figure 8 shows the temperature variation of $\gamma = A_s/A_f$. It can be seen that γ decreases exponentially with increasing temperature. In the low-temperature region below $-93°C$, γ is large, i.e., the ratio of water molecules with slow dynamics to those with fast dynamics is large. The results are consistent with a previous study showing that most of the adsorbed water molecules form domains consisting of the ordered structures and a few water molecules behave as domain wall areas consisting of the disordered structures in this low-T range [15]. On the other hand, from $-73°C$ to $-13°C$, the number of slow-dynamics water molecules is almost equal to the number of fast-dynamics water molecules, and above $-13°C$, the water molecules with fast dynamics are dominant, but the water molecules with slow dynamics have not completely disappeared. However, the existence ratio is small due to the extremely short lifetime of the domains. These results show that the domain size decreases with increasing temperature due to thermal fluctuations. Thus, the two terms with different rates of relaxation of the double exp function correspond to two structures, ordered and disordered structures, and these structures change continuously in the solid–liquid crossover region.

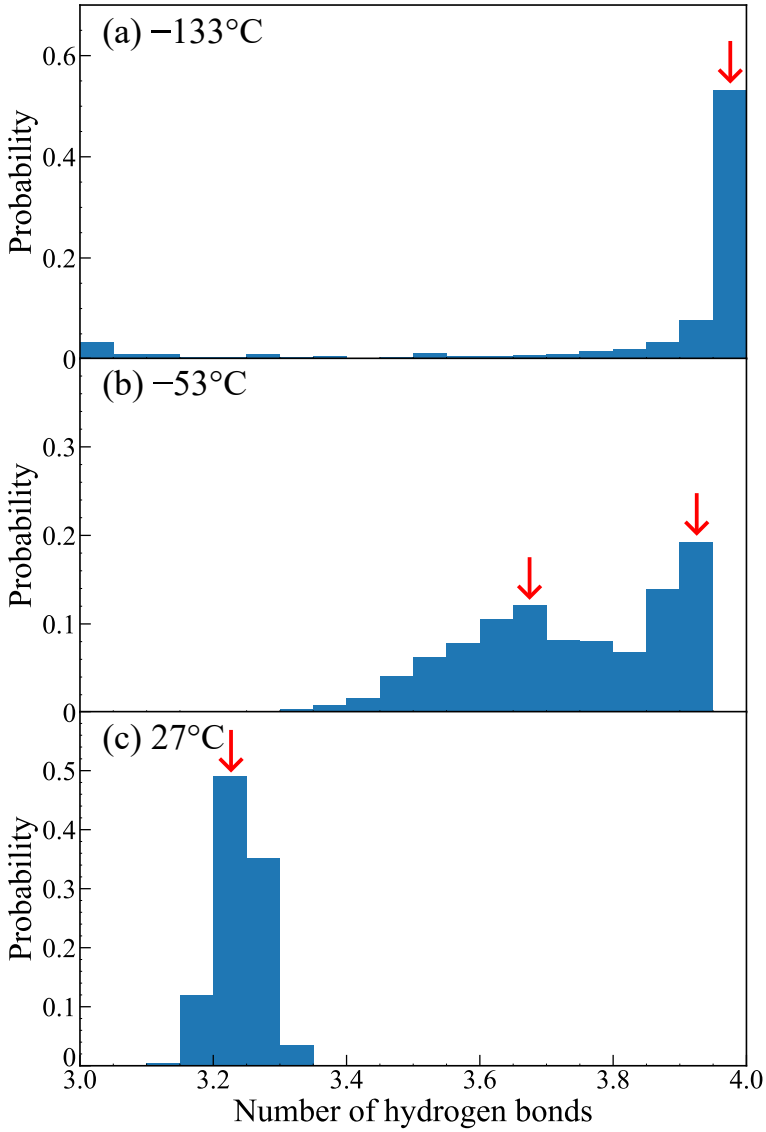

Fig 9. Histograms of average number of hydrogen bonds per water molecule in interfacial water around (13,0) SWCNT at temperatures of: (a) $T = -133$°C, (b) −53°C and (c) 27°C. Copyright 2023 The Japan Society of Applied Physics [43].

3.3.4 Number of hydrogen bonds per molecule

In this subsection, we provide a numerical basis for our speculation in the previous subsection by counting the number of hydrogen bonds per water molecule in the interfacial water around the CNT. In the present study, the hydrogen bonds are defined as those for which the distance between oxygen atoms is less than 0.35 nm and the OOH angle is less than 30° [53].

Figure 9 shows a histogram of the hydrogen-bond number, n, existing in the interfacial water around a (13,0) SWCNT at (a) $T = -133$°C where $\gamma \gg 1$, (b) $T = -53$°C where $\gamma \sim 1$ and (c) $T = 27$°C where $\gamma \ll 1$. As can be seen in Fig. 9(a), a single peak appears near $n = 4$, which corresponds to the domain with the ordered structures. When the temperature is increased to $T = -53$°C, where $\gamma \sim 1$, two peaks (a higher peak at $n \sim 4$ and a lower peak at $n < 4$) appear, indicating the coexistence of ordered structures with slow dynamics and disordered structures with fast dynamics. When the temperature is further increased to $T = 27$°C, where $\gamma \ll 1$, the peak at $n \sim 4$ disappears and a peak appears at a lower position, $n \sim 3.2$. This gradual change in the histogram corresponds to a gradual change from the ordered phase with slow dynamics to the disordered phase with fast dynamics. On the other hand, the number of hydrogen bonds in bulk water had a single peak, and the peak gradually shifted toward a lower with increasing temperature (Appendix C).

3.4 Summary

In conclusion, we calculated the RACF for interfacial water around a (13,0) SWCNT using an MD simulation. The RACF for interfacial water was found to change gradually, and this indicates that the interfacial water does not undergo a clear solid–liquid phase transition. The absence of a solid–liquid phase transition as obtained by MD simulation confirms the recent experimental results obtained by PL spectroscopy [18].

Some previous studies have revealed that the water molecules on graphitic surfaces have two different structures; one is a polygonal cluster forming domains, and the other is a disordered structure within domain wall areas. Therefore, the RACF can be approximated by a double exp function. The decrease in the amount of water molecules with slow dynamics with increasing temperature is consistent with the decrease in domain size. This indicates that water molecules with slow dynamics correspond to water molecules forming the domain and fast dynamics correspond to water molecules forming the domain wall areas. Then, the ratio of domains to domain wall areas gradually decreases with increasing temperature, and water molecules with disordered structures become dominant.

These results reveal, for the first time, the structure of interfacial water around a CNT in the solid–liquid crossover region from the dynamics of water molecules. The RACF approach to rotational dynamics should be useful to investigate the phase transition of water confined inside an SWCNT because it is an interesting low-dimensional system [54–61]. Such work is left for a future study.

4 Electric field response of interfacial water between graphene and h-BN substrates, a property related to water dynamics

4.1 Introduction

Previous studies have shown that the dielectric constant of 1 nm-thick confined water is $\varepsilon_{\mathrm{r}} \sim 2.1$ [20], which is much smaller than that of bulk water at room temperature ($\varepsilon_{\mathrm{r}}^{\mathrm{bulk}} \sim 80$) [21, 22]. With increasing thickness of the confined water, the dielectric constant increases gradually and becomes almost the same as that of bulk water when the thickness reaches ~200 nm.

In this section, we attempt to reproduce the unique dielectric response of water molecules confined in a nanospace from the linear response region to saturation polarization using an atomistic simulation approach. In addition, we give a physical origin of the significant change in dielectric constant from the confined water to bulk water. Some studies have shown that water adsorbed onto a graphitic surface and h-BN substrate surface has a unique structure and properties [8–15, 17, 62]. Thus, the purpose of this section is to clarify the characteristic feature of the dielectric constant of the confined water from the viewpoint of the nanoscale structure and dynamics of confined water.

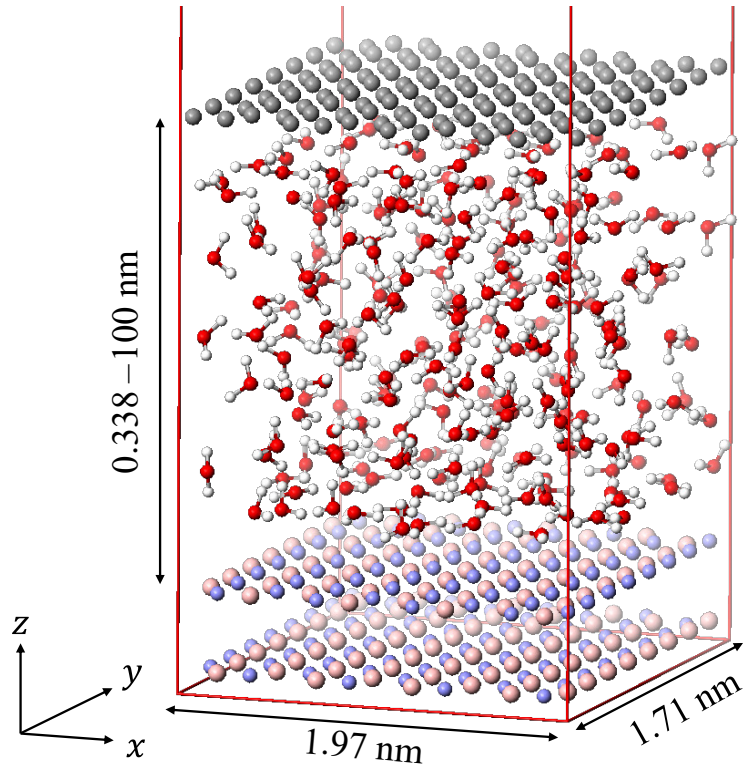

Fig 10. Simulation cell for the graphene/water/h-BN model. The thickness of confined water between the graphene and h-BN surface was varied from 0.338 to 100 nm. Copyright 2023 The Japan Society of Applied Physics [63].

4.2 Simulation model and methods

4.2.1 MD simulation settings and model

We theoretically investigate the dielectric properties of the confined water in the nanospace between graphene and a h-BN substrate through a MD simulation under an electric field applied perpendicular to the substrate. We used the MD simulation package LAMMPS (3 Mar 2020) [40] to investigate the confined water with an electric field applied perpendicular to the substrate. All of the simulations were calculated using the NVT ensemble, and we controlled the temperatures of the system (300 K) using the Nosé–Hoover thermostat [36, 37]. The cross-sectional area in the x–y direction of the simulation box was 1.71×1.97 nm^2; the thickness between the graphene and substrate was varied from 0.338 to 100 nm

and was filled with water molecules (Fig. 10). We determined the thicknesses as the distance where the minimum energy is reached by gradually moving the graphene closer to the h-BN substrate (1.0×10^{-6} nm/fs) confining a given number of water molecules in the nanospace. The length of the simulation box in the z direction is much longer than the cutoff distance of 0.85 nm. We imposed periodic boundary conditions in the (x, y, z) directions. We used SPC/E for the rigid water model [29] and the UFF potential for the force fields between water and other molecules [28]. The equation of motion was numerically solved using the Velocity-Verlet method [27] with $\Delta t = 0.5$ fs. Long-range Coulomb interactions were treated using the Ewald method [38]. The h-BN charges were set to 1.97×10^{-19} C for boron and -1.97×10^{-19} C for nitrogen [62].

4.2.2 Orientational polarization

The SPC/E model used in this study is a rigid body model, and there is no dielectric polarization due to the electric field, only orientational polarization due to permanent dipole moments. We discuss the electric field response of polarization when only orientational polarization is considered. Assuming that the distribution of permanent dipole moments follows a Boltzmann distribution, the number of dipoles dn such that the angle between the electric field E and the permanent dipole moment $\boldsymbol{m}_\mathrm{p}$ is between some angle θ and $\theta + d\theta$ is given by

$$dn = A \exp(-U/k_\mathrm{B}T) d\Omega, \tag{30}$$

note that k_B is the Boltzmann constant, T is the temperature, $d\Omega$ is the solid angle to $d\theta$, U is the potential energy and $U = -\boldsymbol{m}_\mathrm{p} \cdot \boldsymbol{E} = -m_\mathrm{p} E \cos\theta$, and A is the proportionality constant. Since the solid angle $d\Omega$ is equal to the area of the unit sphere between θ and $\theta + d\theta$, it is the product of the circumference length $2\pi \sin\theta$ and the width of the circular

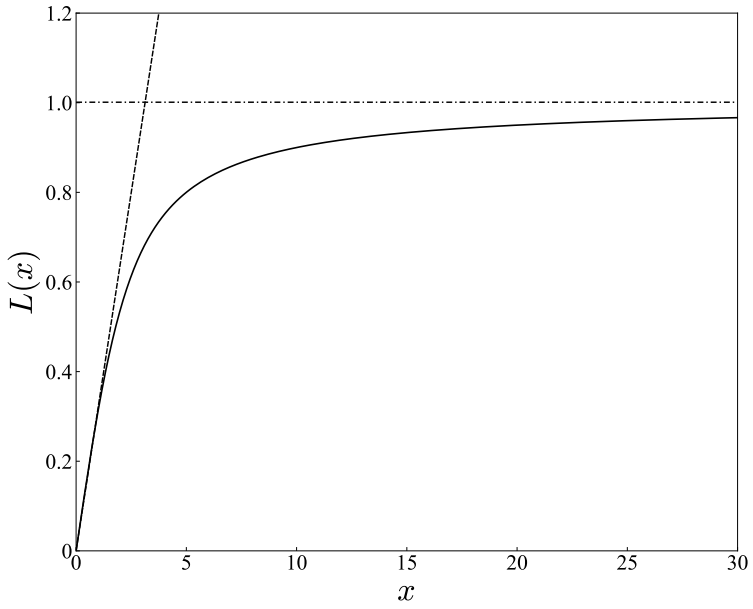

Fig 11. Variation of the Langevin function $L(x)$ concerning $x = m_p E/k_B T$. At constant temperature T, the horizontal axis corresponds to the electric field strength. In the weak electric field region, the Langevin function varies linearly with a slope of $x/3$ (dotted line) and saturates to a maximum value of 1.0 (dashed line) in the strong electric field region.

area $d\theta$ and it is expressed as follows

$$d\Omega = 2\pi \sin\theta d\theta. \tag{31}$$

The probability $p(\theta)d\theta$ that the dipole moment takes the direction θ and $\theta + d\theta$ is

$$p(\theta)d\theta = \frac{A\exp(-U/k_{\mathrm{B}}T)d\Omega}{\int_0^\pi A\exp(-U/k_{\mathrm{B}}T)d\Omega} = \frac{\exp(m_{\mathrm{p}}E\cos\theta/k_{\mathrm{B}}T)\sin\theta d\theta}{\int_0^\pi A\exp(m_{\mathrm{p}}E\cos\theta/k_{\mathrm{B}}T)\sin\theta d\theta}. \tag{32}$$

The mean value of the electric field $\boldsymbol{E}$-directed component of the permanent dipole moment $\langle(\boldsymbol{m}_{\mathrm{p}})_E\rangle$ is

$$\langle(\boldsymbol{m}_{\mathrm{p}})_E\rangle = m_{\mathrm{p}}\int_0^\pi \cos\theta p(\theta)\, d\theta. \tag{33}$$

The magnitude of the orientational polarization P_{p} is the number density of the permanent dipole moments n_{p} times this average. From Eq. (32) and Eq. (33) the magnitude of the

orientational polarization P_p is expressed as follows

$$P_\mathrm{p} = \frac{n_\mathrm{p} m_\mathrm{p} \int_0^\pi \cos\theta \exp(m_\mathrm{p} E \cos\theta / k_\mathrm{B} T) \sin\theta d\theta}{\int_0^\pi \exp(m_\mathrm{p} E \cos\theta / k_\mathrm{B} T) \sin\theta d\theta}, \tag{34}$$

the denominator is the number of dipoles per unit volume, so it is removed from the integral. Now, if $\cos\theta = y$ and $m_\mathrm{p} E / k_\mathrm{B} T = x$, then Eq. (34) is as follows

$$P_\mathrm{p} = n_\mathrm{p} m_\mathrm{p} \frac{\int_{-1}^{1} y e^{xy} dy}{\int_{-1}^{1} e^{xy} dy}. \tag{35}$$

Integrating the numerator by parts, Eq. (35) becomes

$$P_\mathrm{p} = n_\mathrm{p} m_\mathrm{p} \frac{\left[\frac{1}{x} y e^{xy}\right]_{-1}^{1} - \frac{1}{x}\int_{-1}^{1} e^{xy} dy}{\frac{e^x - e^{-x}}{x}} = n_\mathrm{p} m_\mathrm{p} \frac{\frac{e^x + e^{-x}}{x} - \frac{e^x - e^{-x}}{x^2}}{\frac{e^x - e^{-x}}{x}} = n_\mathrm{p} m_\mathrm{p} L(x), \tag{36}$$

where $L(x)$ is the following Langevin function

$$L(x) = \frac{e^x + e^{-x}}{e^x - e^{-x}} - \frac{1}{x} = \coth x - \frac{1}{x}. \tag{37}$$

$L(x)$ and P_p are approximated when $x \ll 1$, i.e., when the electric field is small, as follows

$$L(x) = \coth x - \frac{1}{x} = \frac{1}{x} + \frac{x}{3} - \frac{x^3}{45} + \cdots - \frac{1}{x} \sim \frac{x}{3}, \tag{38}$$

$$P_\mathrm{p} = \frac{n_\mathrm{p} m_\mathrm{p}^2 E}{3 k_\mathrm{B} T}. \tag{39}$$

Thus, the change in orientational polarization concerning the electric field is linear in the weak electric field region, as shown in Fig. 11, and in the strong electric field region the dipoles begin to align completely and the orientational polarization saturates.

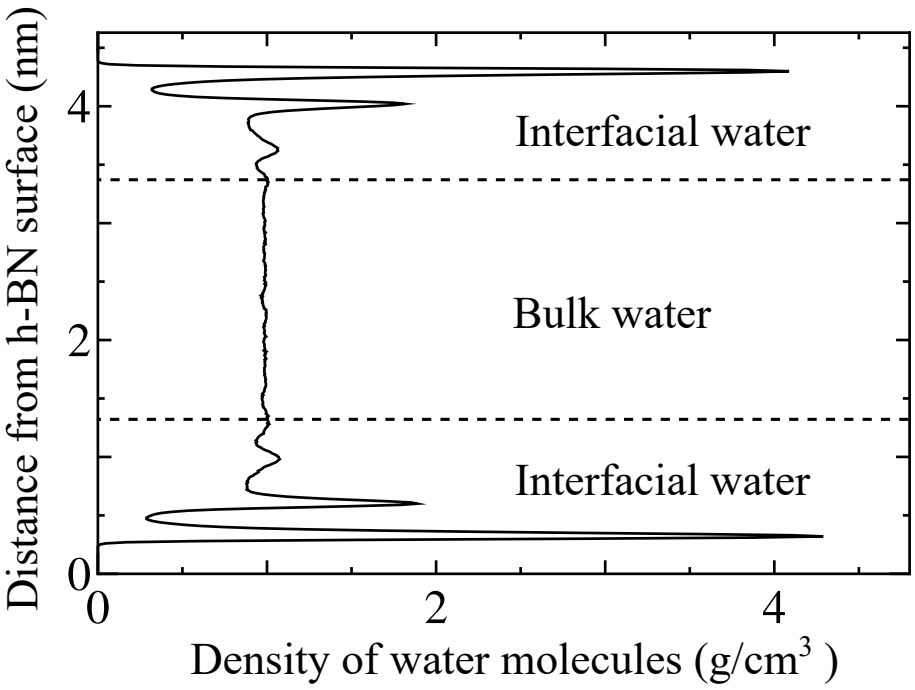

Fig 12. Density distribution of water molecules in confined water with 4.27-nm thickness sandwiched between the graphene layer and the h-BN substrate. The origin of the vertical axis is considered the h-BN surface. Copyright 2023 The Japan Society of Applied Physics [63].

4.3 Results and discussion

4.3.1 Structures of the confined water

We first discuss the microscopic structure of the confined water calculated by MD simulation. Figure 12 presents the averaged density distribution of water molecules in the confined water with 4.27-nm thickness sandwiched between the graphene and the h-BN substrate at 300 K. The origin of the vertical axis in the figure is considered the h-BN surface; the graphene is located 4.63 nm above the h-BN surface. The thickness of the confined water is determined on the basis of the distance between the graphene and the h-BN surface minus the van der Waals radii of carbon and boron atoms.

Figure 12 also shows the three peaks within 1 nm thickness from both of the surfaces;

the two regions can thus be regarded as interfacial water. By contrast, the region 1 nm away from the two surfaces is regarded as a bulk region in which the density is consistent with that of bulk water. The obtained 1 nm thickness of interfacial water near the graphene or h-BN surface is consistent with previous MD results [15, 17, 62]. Hereafter, we refer to these three peaks as the first, second, and third layers of interfacial water, in order from the surfaces. The densities of the first and second layers near the h-BN surface are 4.29 and 1.89 g/cm^3, respectively, whereas those of the first and second layers near the graphene are 4.09 and 1.81 g/cm^3, respectively. The third layer is partially cohesive due to hydrogen bonding with the dense second layer and is slightly denser than the bulk water region [17]. The first and second peaks near the h-BN surface are slightly larger than those near the graphene, as presented in Ref. 62. This difference in peak intensity arises because the van der Waals interaction among the water molecules and h-BN substrate is slightly stronger than that among the water molecules and graphene.

4.3.2 Dielectric response for the weak electric field

In the weak electric field E, electric polarization $P(E)$ of the confined water can be described by $P(E) = \varepsilon_0 \chi E$, where ε_0 is the dielectric constant of vacuum and χ is the electric susceptibility. The electric polarization $P(E)$ is expressed in terms of the dipole moment per unit volume, which is given by,

$$P(E) = \frac{M}{V} = \frac{m}{V} \sum_{i=1}^{N} \cos\theta_i, \tag{40}$$

where V is the volume of confined water, as obtained by subtracting the van der Waals radius of carbon and boron atoms from the thickness between the h-BN substrate and the graphene, and M is the total dipole moment ($M = m \sum_{i=1}^{N} \cos\theta_i$). Here, m ($= 7.83 \times 10^{-28}$ C m) is the magnitude of the dipole moment of a water molecule, θ_i is the angle between the z-axis and the dipole moment of the i-th water molecule, and N is the number of water

molecules. Therefore, the total dipole moment M is $M = VP(E) = V\varepsilon_0\chi E$ and responds linearly to the electric field E, leading to the following relationship from linear response theory,

$$V\varepsilon_0\chi = \frac{1}{k_{\mathrm{B}}T}\{\langle M^2\rangle - \langle M\rangle^2\}, \tag{41}$$

where k_{B} is the Boltzmann constant and T is the temperature of the system. The averages $\langle M\rangle$ and $\langle M^2\rangle$ in Eq. (41) were calculated as the long-time average of the system in the zero electric field. Thus, the electrosensitivity χ is as follows, [64–66]

$$\chi = \frac{1}{Vk_{\mathrm{B}}T\varepsilon_0}\{\langle M^2\rangle - \langle M\rangle^2\}. \tag{42}$$

Note that the electric susceptibility χ is connected to the relative dielectric constant ε_r via the relation $\chi = \varepsilon_r - \varepsilon_\infty$. ε_∞ obtained from the following Clausius–Mossotti equation,

$$\frac{\varepsilon_\infty - 1}{\varepsilon_\infty + 2} = \frac{4\pi\alpha}{3\langle v\rangle}, \tag{43}$$

where v is the volume of the molecule and α is the polarizability, but in SPC/E, the rigid non-polarizable model used this study, $\alpha = 0$, so $\varepsilon_\infty = 1$, and Eq. (42) is transformed as follows [67, 68],

$$\varepsilon_r = 1 + \frac{1}{Vk_{\mathrm{B}}T\varepsilon_0}\{\langle M^2\rangle - \langle M\rangle^2\}. \tag{44}$$

Figure 13 (a) shows the thickness dependence of the relative dielectric constant $\varepsilon_{\mathrm{r}}(h)$ of the confined water, where h is the thickness of the confined water. Within a thickness of a few nanometers, the dielectric constant is $\varepsilon_{\mathrm{r}}(h) \sim 2$, which is much smaller than our calculated dielectric constant for bulk water ($\varepsilon_{\mathrm{r}}^{\mathrm{bulk}} = 72.89$, which is in good agreement with the results of previous studies [69, 70]). As the thickness increases, ε_{r} approaches the relative dielectric constant of bulk water. This thickness dependence is consistent with the experimental results in Ref. 20.

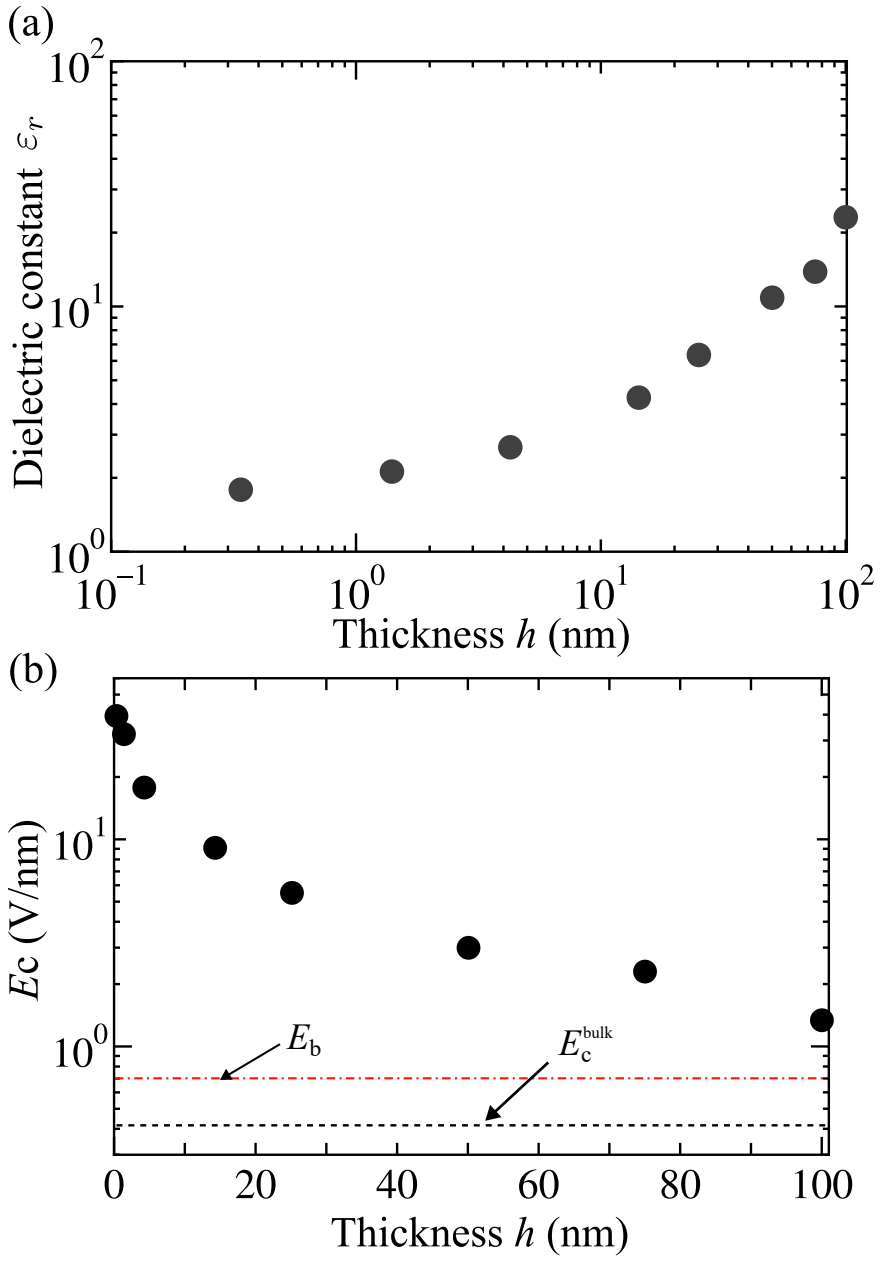

Fig 13. (a) Thickness dependence of the dielectric constant of confined water between the graphene and the h-BN substrate. (b) Thickness dependence of the characteristic electric field $E_c(h)$ for the confined water sandwiched between the graphene and the h-BN substrate. The dotted line ($E_c^{bulk} = 0.416$) indicates the characteristic electric field of the bulk water. The red dashed line ($E_b = 0.7$ [25]) indicates the breakdown electric field of the h-BN substrate. Copyright 2023 The Japan Society of Applied Physics [63].

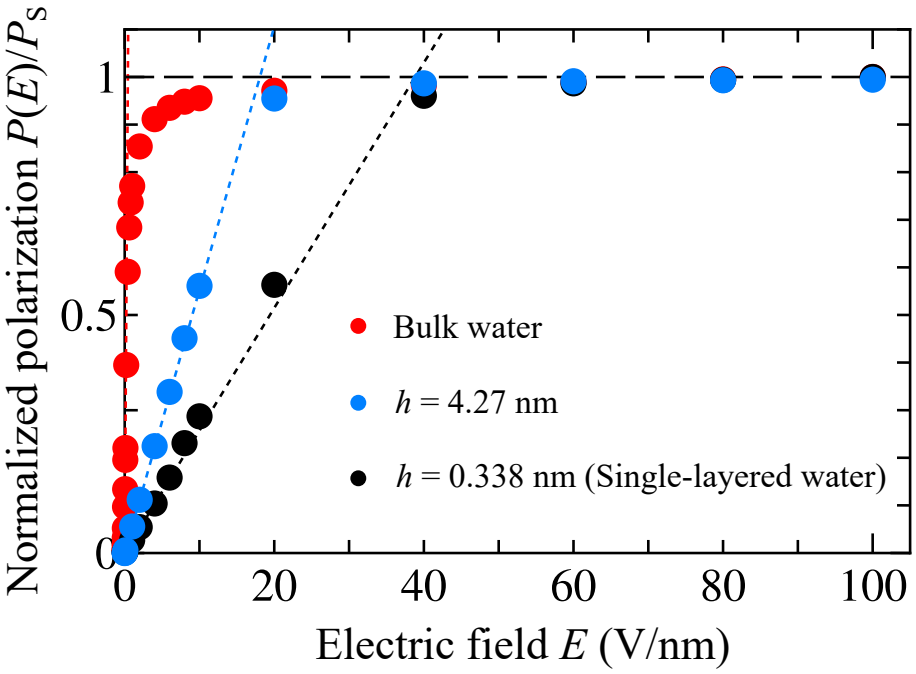

Fig 14. Polarization of confined water with $h = 0.338$ nm (black circles), $h = 4.27$ nm (blue circles), and bulk water (red circles) as a function of the strength of the applied electric field. The vertical axis represents the polarization $P(E)$ normalized by the saturation polarization value P_S. The black, blue, and red dotted lines represent $P(E) = \varepsilon_0 \chi E$ with $\chi = 0.79$ for $h = 0.276$ nm, $\chi = 1.64$ for $h = 4.27$ nm, and $\chi = 71.89$ for bulk water, respectively. The dashed line indicates the fully polarized value $P(E)/P_S = 1$. The characteristic electric field is given by $E_c(h) = P_S(h)/\varepsilon_0 \chi(h)$. Copyright 2023 The Japan Society of Applied Physics [63].

4.3.3 Dielectric response beyond linear response

In Sec. 4.3.2, we discussed the dielectric response of confined water in a weak electric field, wherein polarization can be described by $P(E) = \varepsilon_0 \chi E$. Meanwhile, in the limit of a strong electric field, the water is fully polarized as $P(E) = Nm/V (\equiv P_S)$. Thus, the characteristic electric field is given as

$$E_c = \frac{N}{V} \frac{m}{\varepsilon_0 \chi(h)}, \tag{45}$$

and the system shows crossover from the weak electric field regime to the strong one through $E = E_c$. The h dependence of $E_c(h)$ is presented in Fig. 13 (b). In the limit of $h \to \infty$, the characteristic electric field approaches $E_c^{\mathrm{bulk}} = 0.416$ V/nm of the bulk water (refer to the dashed line in Fig. 13 (b)). The breakdown electric field E_b of the h-BN substrate is important for evaluating the effect of confined water on the transport characteristics of a graphene FET. If E_b is higher than $E_c(h)$, the confined water alters the graphene FET characteristics. As shown in Fig. 13 (b), E_c for confined water with $h < 100$ nm is much higher than $E_b = 0.7$ V/nm for the h-BN [25]; therefore, the confined water with $h \leq 100$ nm does not affect the graphene FET characteristics.

We calculate the $P(E)$ of confined water by calculating $P(E) = \frac{m}{V} \sum_{i=1}^{N} \cos\theta_i$ through an MD simulation with an electric field applied. Figure 14 shows $P(E)$ for several thicknesses, where $P(E)$ is normalized by each saturation value P_S. In the figure, the dotted lines represent $P(E) = \varepsilon_0 \chi E$ obtained by Eq. (42); they coincide with the polarization results obtained by the MD simulation under a weak electric field. In addition, we confirm that the systems exhibit crossover from the weak electric field regime to the strong one across $E = E_c$. Thus, we have succeeded in theoretically reproducing the polarization of the confined water from weak to strong electric fields in the nanospace between graphene and a h-BN substrate.

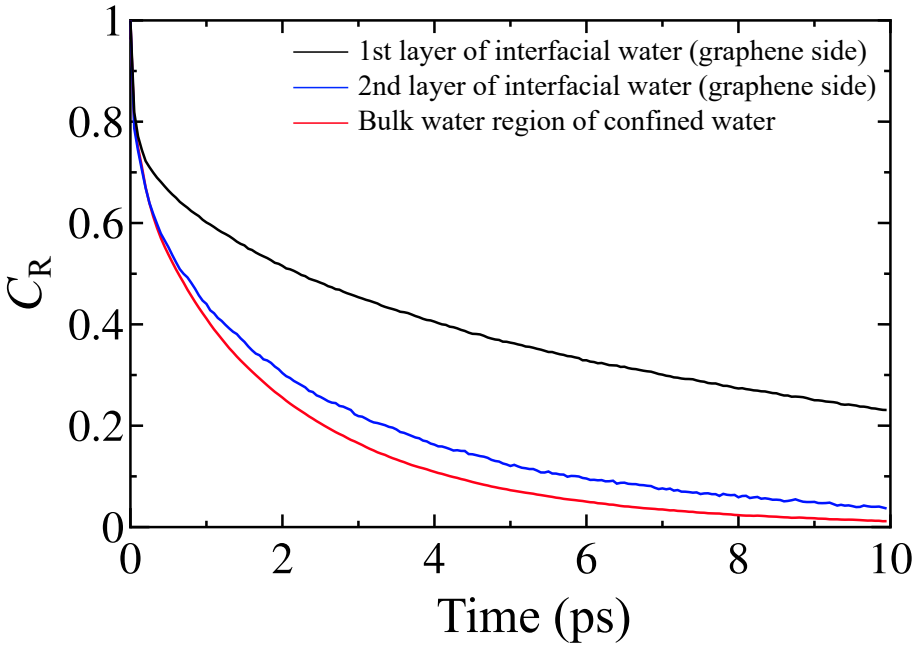

Fig 15. The solid black line is the RACF of water molecules in the first layer (4.2–4.4 nm) on the graphene side of Fig. 12, the solid blue line is the RACF of water molecules in the second layer (3.9–4.2 nm) on the graphene side, and the solid red line is the RACF of water molecules in the bulk water region of confined water (1.4–3.4 nm). Copyright 2023 The Japan Society of Applied Physics [63].

4.3.4 Rotational dynamics and OH bond structures of confined water

Because the static dielectric constant is the real part at angular frequency 0 of the complex dielectric relaxation spectrum represented by the Fourier transform of the time correlation function of the total dipole moments [71], the rotational motion of water molecules is closely related to the dielectric spectrum. We calculated the RACF (Eq.(28)) of water molecules to clarify the degrees of rotational dynamics in each region of the confined water [41, 42].

Figure 15 shows the RACF results for each region in the $h = 4.27$ nm confined water. The RACF in the first water layer on the graphene surface relaxes more slowly than that in the bulk water region, and the correlation with the initial time persists longer. The

RACF in the second water layer relaxes faster than that in the first layer but slightly slower than that in the bulk water region. That is, the interfacial water has a limited degree of rotational freedom compared with the water in the bulk water region. Note that the RACF results for the first and second layers on the h-BN surface are essentially similar to the results for the first and second layers on the graphene surface.

To understand the origin of the rotational dynamics limitation of water molecules in the interfacial water, we examined the orientation of the OH bond of the confined water on the graphene side. Figure 16 shows the distribution of OH bonds in confined water with $h = 4.27$ nm. Angle ϕ represents the angle between the unit vector in the z-axis direction and the OH bond of the water molecules. When $\cos\phi = 1$, the OH bond is oriented toward the z-axis; when $\cos\phi = 0$, it is horizontal to the z-axis; and when $\cos\phi = -1$, it is oriented in the opposite direction to the z-axis.

Figure 16(a) shows that the distribution in the bulk region is completely random, which indicates that the water molecules are in free rotational motion. Therefore, the RACF in the bulk region relaxes extremely quickly (Fig. 15). By contrast, the distribution of OH bonds in the second layer (Fig. 16(b)) and the first layer (Fig. 16(c)) on the graphene side is not random. Figure 16(b) shows that the distribution of the second water layer has a peak at $\cos\phi = 1$; thus, the number of OH bonds oriented to the first water layer increases. This effect is attributed to the water molecules in the second layer forming hydrogen bonds with those in the first layer. Therefore, compared with the structure of the bulk water region, the structure of the second water layer is slightly restricted in its freedom of rotation. The distribution of the first layer has two peaks: one at $\cos\phi = -1$ and another near $\cos\phi = 0$ (Fig. 16(c)). The former peak indicates that water molecules in the first layer interact via hydrogen bonding with the water molecules in the second layer, whereas the latter peak indicates that the water molecules interact via hydrogen bonding within the first layer in a direction parallel to the graphene interface. Hydrogen bonds between water

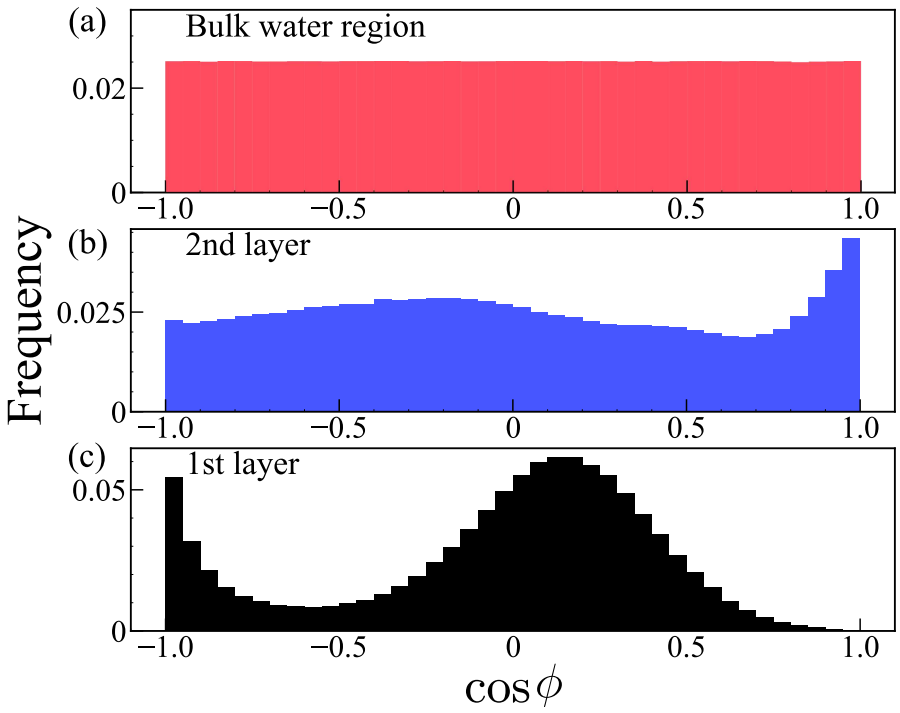

Fig 16. Distribution of OH bond orientations of confined water with $h = 4.27$ nm in (a) the bulk water region, (b) the second layer on the graphene side, and (c) the first layer on the graphene side. Copyright 2023 The Japan Society of Applied Physics [63].

molecules in the same layer and between water molecules in the first and second layers lead to orientation of the water molecules, limiting their freedom of rotational motion. Note that the slightly positive shift from the perfect z-axis parallel direction, $\cos\phi = 0$, occurs because the SPC/E is a rigid model and cannot take $\phi = 90°$ in the case of hydrogen bonding with the water molecules in the second layer. The distribution of OH bonds in the interfacial water on the h-BN substrate side is also almost identical. The third layer had only slightly more hydrogen bonds oriented toward the second layer, but the distribution of OH bonds and RACF results were almost identical to those in the bulk water region.

These results are consistent with those of our previous study which indicated that the interfacial water forms two-dimensional polygonal hydrogen bonds in the plane [15, 17]. Although the water thickness in the present study differs from that in our previous studies,

the distribution of the OH orientation is similar; thus, the thickness h does not strongly depend on the structures and dynamics of the interfacial water, except when h is very thin. According to both our previous study and the present study, the interfacial water has a two-dimensional polygonal hydrogen-bonded structure [15, 17]. The unique structure of interfacial water causes the restriction of its rotational motion, resulting in a small dispersion of the electric dipole moment. Therefore, the dielectric response of the confined water with a few-nanometer thickness is likely to be weaker than that in the bulk water region. The monotonic increase of the dielectric response with increasing thickness h of the water can be explained by a series connection between the dielectric constant of the interfacial water and the bulk water [20].

For extremely thin h with only a single water layer, all OH bonds are parallel to the interface and rotational freedom is limited, resulting in a very low dielectric constant. When the thickness of the confined water becomes sufficiently greater than that of the interfacial water, the dielectric response of the bulk water region begins to dominate and ε_{r} approaches $\varepsilon_{\mathrm{r}}^{\mathrm{bulk}} = 72.89$.

4.4 Summary

In summary, we investigated, through MD simulation, the dielectric response of confined water in the nanospace between graphene and h-BN substrates. We found that the dielectric constant of confined water with nanometer thickness is $\varepsilon_{\mathrm{r}} \sim 2$, which is much smaller than that of bulk water ($\varepsilon_{\mathrm{r}}^{\mathrm{bulk}} = 72.89$). As the thickness h increases, ε_{r} also increases when h exceeds a few nanometers and then approaches $\varepsilon_{r}^{\mathrm{bulk}}$. This h dependence reproduces the previous experimental data reported in Ref. 20. By applying an electric field to the confined water and bulk water, we clarified the polarization properties beyond the linear response region and showed that the behavior in the linear region is consistent with linear response theory. In addition, we found that the saturation electric field P_{S} of the confined water with $h < 100$ nm is much higher than the breakdown electric field of h-BN. This result gives an important perspective for graphene FETs with a h-BN gate insulator: the polarization of confined water does not affect the FET characteristics. Calculations of the RACF and the distribution of OH bonds of confined water revealed that the rotational degrees of freedom of the interfacial water are limited compared with those of the bulk water region. Because the dielectric constant is related to the fluctuations of the electric dipole moment, the limitation of the dynamics might be the cause of the small dielectric constant of the interfacial water. The increase in the thickness h of the confined water, as well as the increase of the dielectric constant ε_{r}, is due to the relative decrease in the fraction of interfacial water compared with the bulk water region. Previous study has hypothesized that the reduction in the dielectric constant of confined water is due to the limited rotational degrees of freedom of the water molecules [20], and the present study demonstrates this hypothesis quantitatively by examining the distribution of RACF and OH bonds.

5 Conclusion

In this thesis, the thermodynamics and electric field response of water confined in the nanospace of a graphitic surface have been studied by analyzing the dynamics and structure of water molecules using MD calculations.

In Section 1, we introduced the fact that water is a familiar substance to us and that water exhibits different properties when bound to a material interface compared to bulk water. In addition, recent studies on the structure and properties of water confined in the nanoscale of a graphitic surface, which is an atomically flat and ideally hydrophobic surface, were also presented.

In Section 2, we introduced the simulation methods mainly used in this study, including the MD calculation algorithm, the potential function, and the thermal control method.

In Section 3, we described a study of the solid–liquid phase transition of water around CNT. Experiments in previous studies have shown that water around CNT does not freeze even when the temperature is lowered to -130°C [18]. We compared the temperature variation of the dynamics of water around CNT with that of bulk water using RACF. As a result, the relaxation speed of RACF changed rapidly around the freezing point of bulk water, confirming the solid–liquid phase transition. On the other hand, the relaxation speed of RACF of water around CNT changed continuously with the temperature change, indicating that the solid–liquid phase transition disappeared as in the experiment. The RACF results can be fitted by a double exp function with a slow relaxation term and a fast relaxation term. These two terms correspond to polygonal and non-polygonal structures, and the ratio of these two structures is found to vary continuously in the solid–liquid crossover region.

In Section 4, we discribed our research on the dielectric properties of water confined at the interface between graphene and h-BN substrates. Recent experimental studies have

reported that the dielectric constant of water confined at the interface between graphene and h-BN substrate is very small [20]. We have reproduced a similar structure by MD calculations and investigated the thickness dependence of the dielectric constant of the confined water. We confirmed that the dielectric constant is very small when the thickness of the confined water is very thin. As the thickness of the confined water is increased, it gradually approaches the dielectric constant of the bulk water. The analysis of the dynamics and structures of the confined water revealed that when the confined water is thin and consists only of interfacial water, the dielectric constant is small because of the rotationally restricted structure. As the thickness increases, the proportion of the bulk water region that can rotate freely increases, and the dielectric constant recovers.

As described above, the structure and dynamics of water reveal the thermodynamics and the electric field response of water aggregated at the graphitic surface. Both phenomena were found to be caused by the layered structure of water near the surface due to the interaction with the surface, which restricts the degree of freedom of rotation. Although we focused on water at atomically flat graphitic surfaces, our method can be applied to the analysis of water at various surfaces. We hope that our method will be applied to the study of water properties at various surfaces such as SiO_2, mica and so on.

Appendices

Appendix A Chirality of CNT

Figure 17 shows a hexagonal lattice of graphene, with carbon atoms at the vertices of a regular hexagon. The vector connecting any two vertices O and A is called the chiral vector $\boldsymbol{C}_h$. This chiral vector $\boldsymbol{C}_h$ can be expressed by using the basic lattice vectors $\boldsymbol{a}_1$ and $\boldsymbol{a}_2$ as

$$\boldsymbol{C}_h = n\boldsymbol{a}_1 + m\boldsymbol{a}_2 \equiv (n, m), \tag{46}$$

where m, n is an integer satisfying $0 \leq |m| \leq n$, and this integer combination (n, m) is called chirality. Note that the chirality of the figure is (4,1). Points B and B' are the points where the line segment perpendicular to the chiral vector from points O and A collides with the vertex of graphene, respectively. Connecting O and A, and B and B', we obtain a cylinder, which is a CNT. Therefore, the chirality determines the winding of the CNT and its structure. When $n = m$ it is called an armchair nanotube, when $m = 0$ it is called a zigzag nanotube, and otherwise it is called a chiral nanotube. The conductivity changes depending on the winding method, and if $(n - m)/3$ is an integer, the nanotube is a metal, otherwise it is a semiconductor.

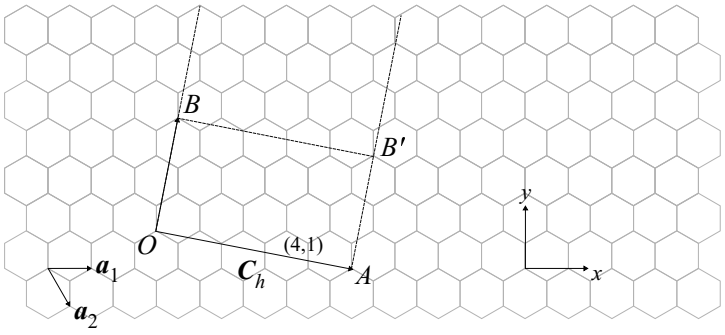

Fig 17. Hexagonal lattice of graphene. The $\boldsymbol{C}_h$ is a (4,1)-chiral vector. The $\boldsymbol{a}_1$ and $\boldsymbol{a}_2$ are the basic lattice vectors of the hexagonal lattice.

Appendix B Terminal values of the RACF for interfacial water around CNT and bulk water

We adopted the terminal value C_{term} of the RACF as an order parameter to distinguish between the liquid and solid phases (*i.e.*, because the system is in the liquid phase when C_{term} relaxes to zero). Figure 18 shows a plot of the C_{term} for water adsorbed onto the CNT surface at various temperatures, together with a plot of the C_{term} for bulk water. The relaxation time of interfacial water is much longer than that of bulk water, especially at low temperatures. Therefore, the value around $t = 30$ ns is considered as the C_{term} and shown in Fig. 18.

In the case of bulk water, the C_{term} decreases abruptly at 0°C as T increases. This result means that the bulk water undergoes a phase transition from the solid phase to the liquid phase at $T = 0$°C. However, in the case of the interfacial water around a CNT, the C_{term} increases gradually around −90°C with decreasing T. The gradual change of C_{term} for the interfacial water around the CNT is totally different from that for the bulk water. This suggests that the interfacial water around a CNT does not undergo a clear solid–liquid phase transition but rather exhibits a solid–liquid crossover.

In addition, the crossover temperature (approximately −90°C) is much lower than the 0°C solid–liquid phase-transition temperature for bulk water. These MD results are consistent with the results of recent experiments based on PL spectroscopy [18].

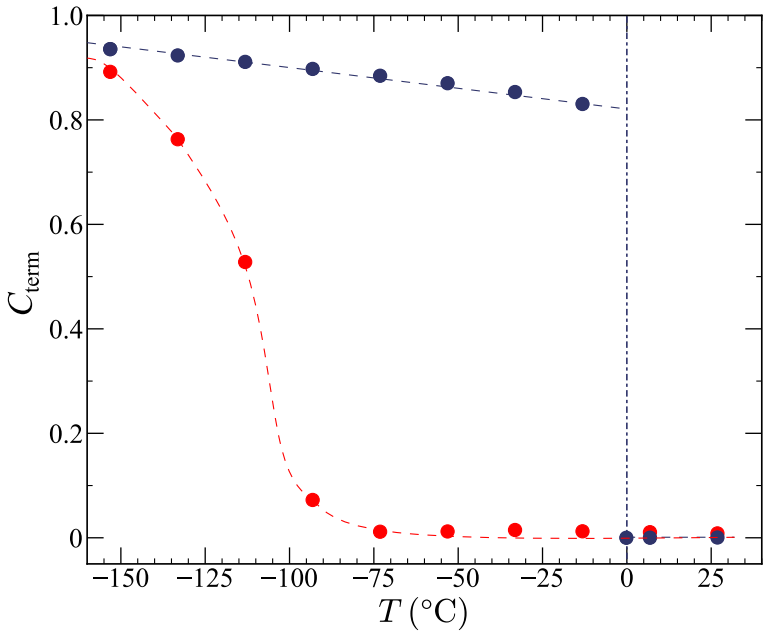

Fig 18. Temperature dependence of the terminal values of the RACF for interfacial water around the (13,0) SWCNT (red marks) and for the bulk water (blue marks). The red and blue dashed curves are provided as guides for the eyes. The vertical broken line indicates T = 0°C. Copyright 2023 The Japan Society of Applied Physics [43].

Appendix C The number of hydrogen bonds per molecule in bulk water

Figure 19 is a histogram of the number of hydrogen bonds per molecule in bulk water. There is no coexistence of two different structures at one temperature as in the results for water around the CNT, but a single peak at all temperatures. At low temperatures below the melting point (Fig. 19 (a)) at $T = -133°C$, most water molecules have a hydrogen bond density of around 4. As the temperature is raised below the melting point (Fig. 19(b)) at $T = 27°C$, the number of water molecules with different numbers of hydrogen bonds increases and the distribution becomes broader. For the temperature increase in the temperature range above the melting point, we confirmed that the peak position shifts towards the one with fewer hydrogen bonds. This corresponds to the disorganization of the hydrogen bond structure of water molecules with increasing temperature and shows the same behavior as in the previous study on the number of hydrogen bonds [72].

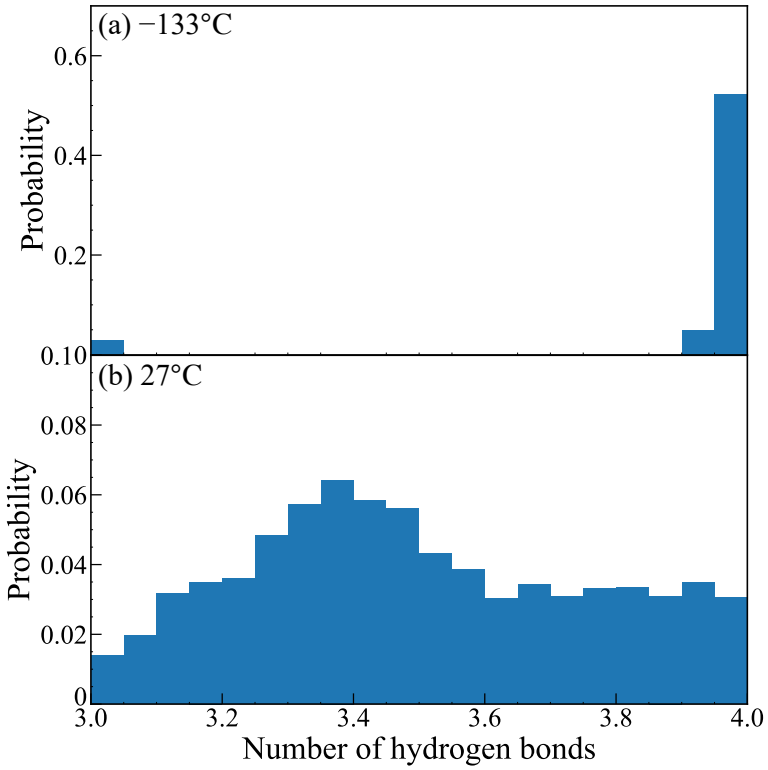

Fig 19. Histograms of average number of hydrogen bonds per water molecule in bulk water at temperatures of: (a) $T = -133$°C, and (b) 27°C

References

[1] J. Russo, K. Akahane and H. Tanaka, Proc. Natl. Acad. Sci. U.S.A. **115**, 15, E3333 (2018).

[2] H. Okajima, M. Ando and H. O. Hamaguchi, Bull. Chem. Soc. Jpn. **91**, 6, 991 (2018).

[3] B. V. Derjaguin, I. I. Abrikosova, and F. B. Leib, Vestnik. Akad. Nauk SSSR, **6**, 125 (1951).

[4] G. Peschel and K. H. Adlfinger, Z. Naturforsch., **26a**, 707-715 (1971).

[5] S. Iijima, Nature **354**, 56-58 (1991).

[6] S. Iijima and T. Ichihashi, Nature **363** 603-605 (1993).

[7] F. M. Fowkes and W. D. Harkins, J. Am. Chem. Soc. **62**, 3377 (1940).

[8] Daniel S. Wastl, Alfred J. Weymouth, and Franz J. Giessibl, ACS Nano **8**, 5233-5239 (2014).

[9] Zhiting Li, Yongjin Wang, Andrew Kozbial, Ganesh Shenoy, Feng Zhou, Rebecca McGinley, Patrick Ireland, Brittni Morganstein, Alyssa Kunkel, Sumedh P. Surwade, Lei Li and Haitao Liu, Nat. Mater. **12**, 925-931 (2013)

[10] K. Xu and J. R. Health, Nat. Mater. **12**, 872-873 (2013).

[11] K. Suzuki, N. Oyabu, K. Kobayashi, K. Matsushige and H. Yamada, Appl. Phys. Express **4**, 125102 (2011).

[12] T. A. Ho and A. Striolo, J. Chem. Phys. **139**, 204708 (2013).

[13] Y. Homma, S. Chiashi, T. Yamamoto, K. Kono, D. Matsumoto, J. Shitaba, and S. Sato, Phys. Rev. Lett. **110**, 157402 (2013).

[14] A. Akaishi, T. Yonemaru, and J. Nakamura, ACS Omega **2**, 2184 (2017).

[15] Y. Maekawa, K. Sasaoka, T. Yamamoto, Jpn. J. Appl. Phys. **57**, 035102 (2018).

[16] K. Suzuki, N. Oyabu, K. Kobayashi, K. Matsushige and H. Yamada, Appl. Phys. Express **4**, 125102 (2011).

[17] K. Kato, Y. Maekawa, N. Watanabe, K. Sasaoka and T. Yamamoto, Jpn. J. Appl. Phys. **59**, 025001 (2020).

[18] Y. Saito, Y. Tanaka, G. Yamaguchi, T. Kato, S. Konabe, S. Chiashi, Y. Homma, J. Appl. Phys. **129**, 014301 (2021).

[19] L. Fumagalli, D. Esteban-Ferrer, A. Cuervo, J. L. Carrascosa, G. Gomila, Nat. Mater. **11**, 808–816 (2012).

[20] L. Fumagalli, A. Esfandiar, R. Fabregas, S. Hu, P. Ares, A. Janardanan, Q. Yang, B. Radha, T. Taniguchi, K. Watanabe, G. Gomila, K. S. Novoselov and A. K. Geim, Science **360**, 1339-1342 (2018).

[21] C. G. Malmberg and A. A. Maryott, J. Res. Natn. Bur. Stand **56**, 1 (1956).

[22] G. A. Vidulich, D. F. Evans, and R. L. Kay, J. Phys. Chem. **71**, 3, 656-662 (1967).

[23] K. I. Bolotin, K. J. Sikes, Z. Jiang, M. Klima, G. Fudenberg, J. Hone, P. Kim and H. L. Stormer, Solid State Commun. **146**, 351 (2008).

[24] K. S. Novoselov, A. K. Geim, S. V. Morozov, D. Jiang, Y. Zhang, S. V. Dubonos, I. V. Grigorieva and A. A. Firsov, Science **306**, 5696 (2004).

[25] C. R. Dean, A. F. Young, I. Meric, C. Lee, L. Wang, S. Sorgenfrei, K. Watanabe, T. Taniguchi, P. Kim, K. L. Shepard and J. Hone, Nat. Nanotechnol. **5**, 722 (2010).

[26] K. Nagashio, T. Yamashita, T. Nishimura, K. Kita, and A. Toriumi, J. Appl. Phys. **110**, 024513 (2011).

[27] W. C. Swope and H. C. Andersen, J. Chem. Phys. **76**, 637 (1982).

[28] A. K. Rappe, C. J. Casewit, K. S. Colwell, W. A. Goddard III, and W. M. Skiff, J. Am. Chem. Soc. **114**, 25, 10024-10035 (1992).

[29] H. J. C. Berendsen, J. R. Grigera, and T. P. Straatsma, J. Phys. Chem. **91**, 24, 6269-6271 (1987).

[30] M. Orsi, Mol. Phys. **112**, 1566 (2014).

[31] M. Holz, S. R. Heil, and A. Sacco, Phys. Chem. Chem. Phys. **2**, 4740 (2000).

[32] H. Dorrani and A. Mohebbi, J. Eng. Thermophys. **32**, 138 (2023).

[33] B. W. Arbuckle and P. Clancy, J. Chem. Phys. **116**, 5090 (2002).

[34] W. L. Jorgensen, J. Chandrasekhar, J. D. Madura, R. W. Impey and M. L. Klein, J. Chem. Phys. **79**, 926–935 (1983).

[35] M. W. Mahoney and W. L. Jorgensen, J. Chem. Phys. **112**, 8910 (2000).

[36] S. Nosé, J. Chem. Phys. **81**, 511-519 (1984).

[37] W. G. Hoover, Phys. Rev. A. **31**, 1695-1697 (1985).

[38] P. P. Ewald, Ann. Phys. **369**, 253 (1921).

[39] R. W. Hockney and J. W. Eastwood, *Computer Simulation Using Particles* (Taylor & Francis,New York, 1988), p.22.

[40] S. Plimpton, J. Comput. Phys. **117**, 1-19 (1995).

[41] Tsun-Mei Chang and Liem X. Dang, J. Phys. Chem. A **112**, 1694-1700 (2008).

[42] K. Singer, J.V.L. Singer, and A.J. Taylor, Mol. Phys **37**, 4, 1239-1262 (1979).

[43] Y. Kioka, T. Hara, Y. Maekawa, K. Sasaoka, Y. Homma, and T. Yamamoto, Jpn. J. Appl. Phys. **62**, 085003 (2023).

[44] L. A. Baez and P. Clancy J. Chem. Phys., **103**, 8 (1995).

[45] R. Shirakashi, *Water and Biomolecules -Dynamics and Stability-*, J. HTSJ, **44**, 4-8 (2005).

[46] H. Uedaira, Jpn. J. Surg. Meta. Nut., **16**, 5 (1982).

[47] W. Kob, *Supercooled Liquids, the Glass Transition, and Computer Simulations* (Lecture notes for LES HOUCHES 2002 SUMMER SCHOOL - SESSION LXXVII on SLOW RELAXATIONS AND NONEQUILIBRIUM DYNAMICS IN CONDENSED MATTER; Les Houches: July 1-26, 2002), p.5-6.

[48] D. R. Reichman and P. Charbonneau, J. Stat. Mech. Theor. Exp, **2005**, 05 (2005).

[49] A. D. Kulkarni, R. K. Pathak, and L. J. Bartolotti, J. Phys. Chem. A., **109**, 4583-4590 (2005).

[50] S. Maheshwary, N. Patel, N. Sathyamurthy, A. D. Kulkarni, and S. R. Gadre, J. Phys. Chem. A., **105**, 10525-10537 (2001).

[51] R. M. Shields, B. Temelso, K. A. Archer, T. E. Morrell, and G. C. Shields, J. Phys. Chem. A., **114**, 11725-11737 (2010).

[52] C. S. Lin, R. Q. Zhang, S. T. Lee, M. Elstner, Th. Frauenheim, and L. J. Wan, J. Phys. Chem. B., **109**, 14183-14188 (2005).

[53] A. Luzar and D. Chandler, Phys. Rev. Lett., **76**, 928 (1996).

[54] H. Kyakuno, K. Matsuda, Y. Nakai, R. Ichimura, T. Saito, Y. Miyata, K. Hata and Y. Maniwa, Scientific Reports **7**, 14834 (2017).

[55] K. Koga, G.T. Gao, H. Tanaka, X.C. Zeng, Nature **412**, 802 (2001).

[56] G. Hummer, J.C. Rasaiah, J.P. Noworyta, Nature **414**, 188 (2001).

[57] Y. Maniwa, H. Kataura, M. Abe, A. Udaka, S. Suzuki, Y.Achiba, H. Kira, K. Matsuda, H. Kadowaki and Y. Okabe: Chem. Phys. Lett. **401**, 534-538 (2005).

[58] K. Matsuda, T. Hibi, H. Kadowaki and Y. Maniwa, Phys.Rev. B **74**, 073415 (2006).

[59] K. Mochizuki and K. Koga, PNAS **112**, 8221 (2015).

[60] D. Takaiwa, I. Hatano, K Koga, and H. Tanaka, PNAS **105** 39 (2008).

[61] H. Kyakuno, K. Matsuda, H. Yahiro, Y. Inami, T. Fukuoka, Y. Miyata, K. Yanagi, Y. Maniwa, H. Kataura, T. Saito, M. Yumura, and S. Iijima, J. Chem. Phys. **134**, 244501 (2011).

[62] Y. Maekawa, K. Sasaoka, T. Yamamoto, Appl. Phys. Express **12**, 115001 (2019).

[63] Y. Kioka, Y. Maekawa, and T. Yamamoto, Jpn. J. Appl. Phys. **63**, 015002 (2023).

[64] M. Neumann and O. Steinhauser, Chem. Phys. Lett. **106**, 563 (1984).

[65] V. Ballenegger and J.-P. Hansen, J. Chem. Phys. **122**, 114711 (2005).

[66] Douwe Jan Bonthuis, Stephan Gekle and Roland R. Netz, Langmuir **28**, 7679-7694 (2012).

[67] G. Lamoureux, A. D. MacKerell, and B. Roux, J. Chem. Phys. **119**, 5185 (2003).

[68] A. D. Buckingham, Proc. R. Soc. London. Ser. A. Math. Phys. Sci. **238**, 235 (1956).

[69] Orsolya Gereben and László Pusztai, Chem. Phys. Lett., **507**, 80-83 (2011).

[70] Piotr Zarzycki and Benjamin Gilbert, Phys. Chem. Chem. Phys., **22**, 1011 (2020).

[71] D. van der Spoel, P. J. van Maaren and H. J. C. Berendsen, J. Chem. Phys., **108**, 10220-10230 (1998).

[72] D. Prada-Gracia, R. Shevchuk, and F. Rao, J. Chem. Phys. **139**, 1 (2013).

Publication lists

1. ”Coexistence of slow and fast dynamics in interfacial water around a carbon nanotube”

   Yusei Kioka, Takemi Hara, Yuki Maekawa, Kenji Sasaoka, Yoshikazu Homma and Takahiro Yamamoto

   Japanese Journal of Applied Physics, Vol.62, No.8, 085003 (2023).

   DOI:10.35848/1347-4065/aced75

2. ”Molecular dynamics simulation on the dielectric properties of water confined in a nanospace between graphene and a h-BN substrate”

   Yusei Kioka, Yuki Maekawa and Takahiro Yamamoto

   Japanese Journal of Applied Physics, Vol.63, No.1, 015002 (2023).

   DOI:10.35848/1347-4065/ad0cd8